

1 **Title** Self-actuating origamis realized by independently printable and controllable
2 stimuli-responsive creases

3 **Authors** R. Wu,¹ K. W. Kwan,^{1*} W. Ma¹, P. Wang,^{1†}, A. H. W. Ngan¹

4 **Affiliations**

5 ¹Department of Mechanical Engineering, the University of Hong Kong, Pokfulam Road, Hong
6 Kong, P.R. China

7 *Corresponding author, e-mail address: kkwkwan@connect.hku.hk

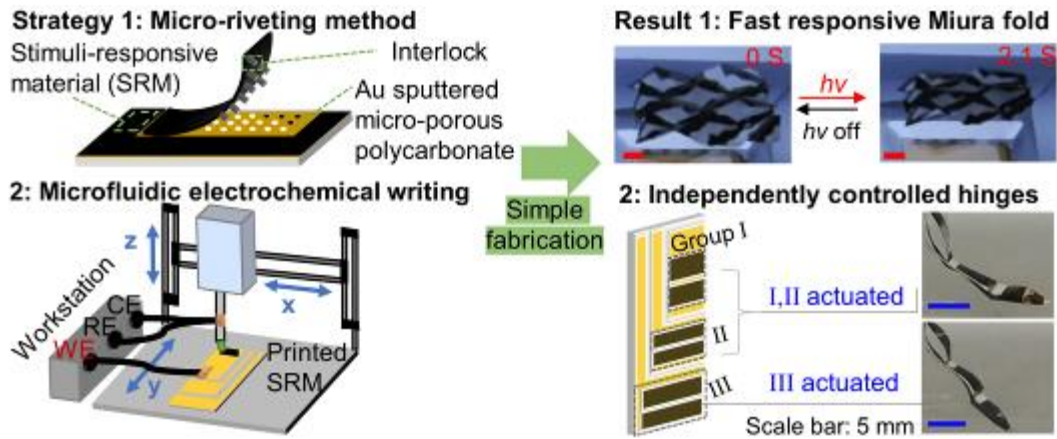
8 †Present address: Department of Materials Science and Engineering, Stanford University, USA

9 **Abstract**

10 Flexible origami structures can mimic the complicated motions of small creatures that are
11 otherwise difficult to be achieved by rigid robots with limited degree of motion freedom.
12 However, actuating origami structures in a compact and self-contained way has been a critical
13 challenge. Here, we demonstrate a versatile approach of actuating origami micro-robots by
14 printed self-folding creases made of a type of stimuli-responsive transition metal
15 hydroxides/oxides that can undergo large actuation under electrochemical or light stimulations.
16 Two enabling technologies are pivotal: (i) a microfluidic electrochemical writing method to
17 selectively print the stimuli-responsive material (SRM) at the actuating creases to enable them to
18 self-fold independently “on demand”, and (ii) a micro-scale riveting method to provide strong
19 adhesion of the SRM on the origami body. Such strategies allow the successful construction of
20 actuating creases made from different stimuli-responsive transition metal hydroxides/oxides that
21 can self-fold into curvature exceeding 1 mm^{-1} under low-intensity visible-light stimulation in
22 ambient conditions, or low-potential electrochemical stimulation in electrolytic environments,
23 with response time as fast as in seconds. Based on the high performance of such active creases,
24 complex miniaturized origami designs powered by hinges activated in an independently
25 controllable way are demonstrated, including self-folding Miura and a full micro-robotic hand

1 with independently programmable finger joints. These results prove a new, versatile paradigm for
2 robotics, where a transferrable approach is applicable to design and fabricate a wide variety of
3 customizable micro-robots with compact construction and complex motions using different
4 stimuli-responsive ceramic-based materials.

5 **Graphic abstract**



6
7 **Keywords:** Micro-origami robotics; Open electrodeposition; Micro-riveting; Transition-metal
8 oxides/hydroxides; Independently controlled micro-hinges; Stimuli-responsive materials

9
10
11
12
13
14
15
16
17
18
19
20
21
22
23
24
25
26
27
28
29
30
31

1 MAIN TEXT

2 Introduction

3 Origami-robots are regarded as next-generation machines that can shape-transform, walk/crawl,
4 and perform tasks over a large domain of the configurational space [1, 2, 3, 4]. The major
5 components of origami designs involve a supporting structure that allows folding and actuating
6 units that induce the shape transformation [5, 6]. Earlier designs of origami robots are powered by
7 discrete motors [7], fluid [8, 9] or magnets [10, 11] which require bulky backing systems or
8 external magnetic field generators, respectively. To increase the compactness level for the
9 complex origami structures containing many faces and hinges, origami designs powered by
10 stimuli-responsive materials (SRMs) have emerged [12-20]. For realistic applications, however,
11 the SRM chosen should be reversible and fast responding, say, in seconds, and the stimuli should
12 be low-power and easily integrable into system designs. Origami designs involving one-way
13 shape memory materials [12], polymers or gels [13, 14, 15] are irreversible in motion or exhibit
14 slow responses from several minutes to hours. Deploying actuating materials responsive to
15 temperature [16, 17, 18] or humidity [19] changes are less practical as these stimuli are less easily
16 integrated into or delivered to compact systems, than stimuli such as electric or light signals.
17 Graphene-based origami robots driven by near infrared (NIR) light can perform fast shape
18 transformation, but their fabrication and stimulation involving graphene and NIR are rather
19 complex [20].

20 Despite the few SRM-powered origamis demonstrated so far, they were designed and
21 fabricated based on protocols specific to the SRM chosen, and hence, a versatile paradigm that is
22 transferrable to different SRMs and designs is critically lacking. In this work, we demonstrate a
23 versatile and simple approach for actuating origamis that has never been attempted before (Fig.
24 1). We construct stimuli-responsive self-folding creases for actuating origamis, as per a
25 “minimalism” concept. An origami robot, by definition, is a structure that changes shape by
26 folding of its creases, and so the “minimalist” design would be to have just the creases, rather than

1 the whole body, made of a high-performing SRM that enables them to self-fold efficiently upon
2 receiving external stimuli (Fig. 1B). Such a design concept, in conjunction with a high-
3 performing SRM, should lead to origamis that are most compact, but its realization would imply
4 overcoming two immediate challenges:

- 5 (i) How to integrate the SRM into the specific locations of the creases “on demand”, so that,
6 for instance, the creases can be stimulated independently of one another, or different
7 crease patterns can be easily made with a single setup?
- 8 (ii) The origami substrate can only be compliant materials like polymers, because metals or
9 ceramics would crack or fatigue-fail on repeated folding. Therefore, it is of paramount
10 importance to ensure enough adhesion between the polymeric substrate and the chosen
11 SRM, so that the latter would not delaminate on repeated folding of the crease.

12 In this study, we aim to demonstrate a versatile approach for solving the above two problems
13 which is in principle applicable to a wide variety of ceramic-based SRMs that can be fabricated
14 by electrodeposition. For the purpose of illustration, we choose a recently discovered type of
15 stimuli-responsive transition metal hydroxides/oxides [21, 22] including nickel
16 hydroxide/oxyhydroxide (NHO, Fig. 1A) or manganese oxides [23], that are fast responding to
17 mild electrochemical or light stimuli. For solving challenge (i) mentioned above, we demonstrate
18 a microfluidic electrochemical writing method for the “on demand” writing of the SRMs on the
19 origami substrate (Fig. 1C(i)). Existing fabrication methods such as selective-laser sintering or
20 ink-jet printing of a ceramic precursor followed by post-treatment [24, 25], or masked
21 electrodeposition [26, 27], can result in ceramic patterns, but the precursor method involves
22 additional sintering which is not applicable to ceramic patterns coated on polymeric origami
23 substrates, and masked electrodeposition requires a new mask for each pattern to be made. Here,
24 we demonstrate a direct and simple open-electrodeposition method, and apply it to the SRMs. For
25 solving challenge (ii) above on adhesion between the SRMs and the origami substrate, we

1 demonstrate a micro-riveting concept (Fig. 1C(ii)), in which the hydroxide/oxide SRMs forms
2 strong locks with micro-porous polycarbonate (MPPC) substrates to provide the adhesion needed
3 for the folding process. These methods are used to successfully fabricate pre-designed crease
4 patterns of SRMs to make self-folding origamis driven by either electrochemical or visible-light
5 stimulations (Fig. 1B). In Results below, the SRMs are first described, followed by the enabling
6 technologies and resultant origamis.

7

8 **Results**

9 **1. The active stimuli-responsive materials**

10 The key concept in the present work is to actuate origamis by independently printable and
11 controllable stimuli-responsive creases, and we demonstrate this using a type of transition metal
12 hydroxides or oxides for the creases that have been recently discovered to exhibit significant
13 volume shrinkage on mild oxidizing potential charging in alkaline electrolytes [21, 23], or under
14 low-intensity light illumination in ambient conditions [22]. In addition to their high-performing
15 actuation behavior (details given below), these materials are also low-cost and easily printable on
16 substrates using electrodeposition (see Methods), so they are ideal for making self-folding
17 origami creases. In below, due to space limitation, we illustrate the working principles using
18 results primarily from nickel hydroxide/oxyhydroxide (abbreviated as NHO, see Fig. 1A),
19 although we also fabricated a robotic hand made of independently printed and controlled MnO_x
20 muscles as shown in Movie S1 and fig. S4A. Both NHO and MnO_x exhibit an electrochemical
21 actuation behavior under mild potential stimuli in alkaline media [21, 23], and in addition, NHO
22 exhibits a light-triggered actuation behavior under low-intensity visible-light stimuli in ambient
23 conditions [22].

24 Although the actuation behavior of transition metal hydroxides/oxides has been reported
25 before [21, 22], how their microstructure changes in response to stimuli is not clear. Therefore, to

1 illustrate the mechanisms of the actuation, we carried out detailed microstructural characterization
2 on NHO, which is the main material presented hereafter. As shown in Fig. 2A, cyclic
3 voltammetry shows that the NHO material can be oxidized on potential larger than ~ 0.4 V and
4 reduced at potentials smaller than ~ 0.3 V against Ag/AgCl reference electrode in 1 M NaOH,
5 depending on the scan rate. Larger scan rates can lead to higher current peak (absolute value) and
6 lower curvature (Fig. 2A and S6). A larger range of scan rate was also studied for the same
7 actuator at a fixed potential window, and again, the curvature drops at increasing scan rate
8 because of incomplete and suppressed redox reaction at higher scan rate (Fig. S7). Figure 2B(a)
9 shows the grazing-incidence X-ray diffraction (GIXRD) spectra of the oxidized and reduced
10 states of NHO. The GIXRD patterns of these two states show characteristic changes near 34° and
11 37° , shown in a magnified scale in Fig. 2B(b), due to the (100) β -Ni(OH)₂ (2.63 Å) and (101) β -
12 NiOOH (2.43 Å) diffractions, respectively [28, 29]. On changing from the reduced to oxidized
13 state, the (101) β -NiOOH peak near 37° emerges, whereas the (100) β -Ni(OH)₂ peak near 34°
14 subsides, indicating that the oxidation is due to the transformation from β -Ni(OH)₂ to β -NiOOH,
15 as shown in Fig. 1A(i). β -NiOOH is known to have a smaller crystal volume than β -Ni(OH)₂ [21,
16 22], and this explains the volume shrinkage on oxidation.

17 Another characteristic of the GIXRD patterns of both the reduced and oxidized states is a
18 broad peak at $2\theta \sim 18^\circ$, which arises from the (001) planes of both the Ni(OH)₂ and NiOOH
19 hexagonal crystal structures [28, 29]. Fig. 2B(a) shows that, on changing from the reduced to
20 oxidized state, the (001) peak becomes sharper, and the 2θ value of $\sim 18^\circ$ corresponds well to the
21 wavy lattice fringes of ~ 4.7 Å in the oxidized state directly observed by HRTEM in Fig. 2C. The
22 wavy nature of the (001) lattice fringes are characteristic of turbostratic crystal structures due to
23 the intercalation of H₂O molecules into the lattice [29, 30] – a fact confirmed by a large H₂O
24 absorption peak observed in Fourier-transform infrared spectroscopy measurements [28]. The
25 observed sharpening of the (001) peak indicates a drop in turbostraticity, or loss of intercalated

1 water from the lattice, on oxidation. As water is lost from the crystal structure, the volume should
2 shrink, and this is likely a second reason for the observed shrinkage on oxidation of NHO [21].

3 As for light actuation, in situ GIXRD experiments were carried out with a visible light source
4 placed inside the diffractometer to excite the NHO sample in the oxidized state, which is the as-
5 fabricated state of the NHO in all the light actuation tests in this work (see Methods). The GIXRD
6 results in Fig. 2B(c) and (d) show that during X-ray scanning at a very slow rate of $0.05^\circ/\text{min}$
7 without or with visible light illumination at intensity $\sim 50 \text{ mW}/\text{cm}^2$, a noticeable change is a slight
8 right-shift of the right edge of the (001) broad peak at $2\theta \sim 18^\circ$ (Fig. 2B(d)). The previously
9 described changes near 34° and 37° on changing from oxidation to reduction were not noticeable
10 during light illumination on the oxidized sample in Fig. 2B(b), indicating that the light excitation
11 only slightly decreases the interplanar spacing of the (001) basal planes, but does not
12 electrochemically reduce the sample. The right shift of the 2θ value on light stimulation was
13 about 0.17° , and from Bragg's law, the (001) plane spacing is reduced by about 0.91% at ~ 50
14 mW/cm^2 illumination. Earlier work has indicated that the light induced shrinkage of NHO only
15 occurs in ambient conditions with regular humidity, but not in a vacuum environment, and the
16 material also exhibits actuation on humidity changes of the environment [21]. The results in Fig.
17 2B(d) now indicate that light illumination reduces the (001) spacing, evidently due to a light-
18 induced loss of the intercalated water molecules from the crystal structure. The light only causes
19 the right edge of the (001) peak to shift right, presumably because visible light can only penetrate
20 into a very shallow layer of the sample surface where the (001) spacing is smaller due to
21 dehydration, while the left edge of the (001) X-ray peak is dominated by deeper layers reachable
22 by X-ray.

24 **2. Enabling technologies**

25 *2.1 Substrate/interface engineering*

1 The key concept of the present work is to integrate the SRM into a suitable origami substrate
2 at specific locations to make self-folding creases (Fig. 1B). As mentioned above, soft polymeric
3 instead of metallic or ceramic films are chosen as the origami substrates since polymers are
4 generally soft enough to be repeatedly foldable. Furthermore, according to Timoshenko's theory
5 [31], for an actuating layer of thickness h_a and elastic modulus E_a coated on top of a passive
6 substrate layer of thickness h_s and elastic modulus E_s , the actuation curvature is given by (see
7 Section S1):

$$\kappa = \frac{6h_a(h_a + h_s)}{E_a h_a^3 + E_s h_s^3} \sigma_a \quad (1)$$

9 where σ_a is the intrinsic actuating stress of the active layer. Eqn. (1) indicates that large actuation
10 will be achieved by lowering the stiffness of the substrate.

11 In this work, a type of thin microporous polycarbonate (MPPC) membranes with pore size 3
12 μm (unless otherwise stated) and thickness $h_s = 10 \mu\text{m}$ was used as the origami substrates. Prior to
13 electrodeposition of the SRM, the MPPC membranes were pre-sputtered with a thin atomic layer
14 of Au (see Fig. 1C and inset in Fig. 3D), which served not only as the conductive electrode for the
15 electrodeposition, but also increased the adhesion between the hydroxide or oxide SRM, and the
16 MPPC. The porous nature of the MPPC membrane serves two purposes. First, the presence of the
17 pores lowers the effective modulus, and hence larger actuation can be achieved according to eqn.
18 (1). Secondly, as the SRM material is deposited onto the MPPC membrane, some of it will grow
19 into the micro-pores of the membrane to form micro-scale rivets as shown in Figs. 3A and 1C(ii),
20 so that the SRM layer will adhere firmly to the substrate. After short electrodeposition for 0.5 h in
21 the case of NHO (Fig. 3A(i)), some of the pores in the MPPC membrane were covered by NHO
22 but others were unfilled, and prolonging the electrodeposition to 2 h (Fig. 3A(ii)) resulted in all
23 pores covered by an NHO layer. To reveal the growth of the NHO material into the pores of the
24 MPPC substrate, peel tests were performed (Fig. 1C(ii)). Peeling off an NHO layer

1 electrodeposited for 2h from the MPPC membrane revealed the deep deposition of the NHO
2 material into the cylindrical pores as shown in micrographs (III) and (IV) in Fig 1C(ii).

3 To show that the micro-riveting strategy is effective in improving the actuating performance,
4 control experiments were carried out on actuators made by electrodepositing NHO onto non-
5 porous polycarbonate (PC) membranes as well as porous ones with different pore sizes. On non-
6 porous PC substrate, the actuation is very small, due to the significant delamination of the active
7 material which can be observed just after five cycles of actuation when the active material was
8 deposited for 0.5h (inset in Fig. 3B). To figure out the influence of the substrate pore size on the
9 adhesion and actuating performance, PC substrates with pore sizes of 0.03, 0.2, 3 and 10 μm were
10 electrodeposited with the NHO material for 0.5 h, 1h and 2 h, as shown in Fig. 3B. Actuators
11 made on the substrate with a pore size of $\sim 0.2 \mu\text{m}$ deliver the best actuating performance, and for
12 the same pore size, prolonging the electrodeposition of the active material from 0.5 h to 2 h leads
13 to improvements in the actuation performance, due to more and deeper filling of the NHO into the
14 substrate pores as shown in Fig. 3A(i) and (ii). To assess the long-term reliability of the micro-
15 riveted NHO/MPPC interface, bilayered actuators made with uniform NHO electrodeposited (for
16 2 h) onto MPPC substrates were subjected to repeated light and electrochemical stability tests (see
17 Materials and Methods). Figure 3C shows the change of the bending angle of the actuators over
18 3000 cycles. The actuation performance was very consistent over long usage under both light and
19 electrochemical stimuli, and only began to degrade after around 2700 cycles for the case of
20 electrochemical actuation, due possibly to cracks formed during repetitive ultra-large motions.
21 Before the final degradation, there was no significant sign of delamination of the NHO material
22 from the MPPC substrate, thus indicating a strong interlocking effect of the micro-rivets into the
23 porous substrate especially at long electrodeposition time.

24 To show the advantageous effect of MPPC as the substrate material, NHO layers of different
25 thickness h_a in the range 0.6 – 2.2 μm were deposited onto 10 μm thick MPPC membranes (see

1 Sections S2 and S3). In Fig. 3D, the bending curvature κ observed under electrochemical
2 actuation tests conducted in 1 M NaOH electrolyte and light stimulation of around 20 mW/cm² is
3 plotted against the factor $6h_a(h_a + h_s)/(E_a h_a^3 + E_s h_s^3)$ according to Eqn. (1). It can be seen that
4 the data fall onto straight lines in agreement with Eqn. (1). Furthermore, data from similar
5 actuators made by depositing NHO onto Ni substrates (with much higher Young modulus of ~220
6 GPa than the ~2.3 GPa for MPPC) are also plotted in Fig. 3D for comparison [21]. It can be seen
7 that the achievable bending curvature on Ni substrates is only up to about 0.2 mm⁻¹, while this can
8 reach 1.2 mm⁻¹ on the MPPC substrates (see Movie S2). As analyzed in Section S2, under
9 electrochemical potential drive of less than 1 V in 1 M NaOH electrolyte, NHO can deliver an
10 intrinsic actuation stress of ~20 MPa over strains up to 1% and work density up to ~100 kJ/m³,
11 which outperforms human muscles with work density of ~40 kJ/m³ [32]. Under low visible light
12 stimulation at ~20 mW/cm², NHO can deliver an intrinsic actuation stress of ~11 MPa at ~0.5%
13 strain with work density about 28 kJ/m³ (see Section S3).

14

15 2.2 Selective printing of actuation patterns

16 To print the SRM onto the origami substrate at specific locations where it is needed, the first
17 method used was masked deposition. Fig. 4A shows this process for the case of the “Miura”
18 origami structure shown in Fig. 1B(ii, iii), where two sets of target NHO crease patterns need to
19 be electrodeposited on the top and bottom sides of an MPPC membrane. However, to improve the
20 flexibility of pattern design and fabrication, a special microfluidic electrochemical writing method
21 involving the local microfluidic delivery of electrolyte [33] was also developed for both the NHO
22 and MnO_x material, as shown in Figs. 1C(i) and 4B. In this method, the required electrolyte for
23 the SRM electrodeposition (see Materials and Methods) is delivered locally to the desired location
24 of the conductive substrate via a pump-driven syringe needle which itself is also conductive. A
25 gap is maintained between the needle tip and the substrate, so that a micro-volume of the liquid

1 electrolyte is held between the two by surface tension effects. Application of a suitable potential
2 difference between the conductive syringe needle and the substrate then triggers the
3 electrochemical formation of the SRM within the small electrolyte volume in contact with the
4 substrate, and scanning the needle over the substrate allows an SRM pattern of any geometry to
5 be written on the substrate. Repeatedly scanning over the same place would also increase the
6 thickness of the SRM deposited.

7

8 **3 Origami actuator performance**

9 *3.1 Self-folding origami structures triggered by light and electrochemical stimulations*

10 The performance of a single crease design under light and electrochemical stimuli is shown in
11 Fig. 1B(i). The samples were fabricated by electrodepositing a 4 mm-wide strip of the NHO
12 material across the width of a rectangular MPPC membrane substrate measuring 16 mm by 8 mm
13 (see Materials and Methods). After the electrodeposition, residual stress caused the membrane to
14 bend to form a smooth crease, as shown in Fig. 1B(i). Under light illumination or oxidizing
15 potential charging, the creases self-actuated in the direction that corresponds to the contraction of
16 the coated NHO material. The bending angle could be up to 120° under light intensity of ~ 40
17 mW/cm^2 , or 160° over the potential window from 0.8 V to -0.2 V with a scan rate of 25 mV/s (see
18 Movie S3). For light actuation, the actuating rate increases from 8.7 deg/s to 60 deg/s for light
19 intensity from $5 \text{ mW}/\text{cm}^2$ to $40 \text{ mW}/\text{cm}^2$, and the corresponding recovery rate increases from 6.5
20 deg/s to 22.5 deg/s. The single origami crease design was triggered by step potential under -1 V
21 for 0.5 s to actuate and 1 V for 1 s to recover in 1 M NaOH electrolyte, or under illumination of
22 vis light intensity at $\sim 25 \text{ mW}/\text{cm}^2$ on for 0.5 s to actuate and 1 s off to recover for both 1000 times.
23 Under both types of stimuli, the actuation performance was very stable over the 1000 cycles (Fig.
24 S8).

1 Based on the single NHO creases, a variety of self-folding origami structures were fabricated
2 and tested. Fig. 5 and Movies S4, S5 and S6 show the self-folding response of Miura origami
3 structures under the stimulation of visible light and electrochemical stimulation. These structures
4 were printed using the method shown in Fig. 4A, and to facilitate their subsequent self-folding
5 action under stimulation of the active NHO, the MPPC substrates were pre-folded along the
6 crease patterns after their printing. In the present work, all the as-fabricated NHO material was in
7 the oxidized state (see Materials and Methods) so that for light actuation, the initial state would
8 *contract* on light stimulation, and for electrochemical actuation, the initial state would *expand* on
9 application of a *reduction* potential (see Fig. 1A). Therefore, to allow the as-fabricated Miura
10 structures to self-fold on application of either light or reduction-potential stimuli, the pre-folding
11 directions were opposite between the two cases: for light stimulation, the solid-line creases
12 printed on the top side of the MPPC membrane in Fig. 4A became folded valleys while the
13 dashed-line creases printed on the bottom became folded mountains when viewed from the top,
14 and for the electrochemical actuation, the folding sense was reversed. In this way, the Miura will
15 shrink on either application of a reduction potential (Fig. 1B(ii)) or light illumination (Fig.
16 1B(iii)).

17 To quantify the Miura actuation, Fig. 5 (A, B) illustrate the schematic of the Miura fold. The
18 parameters α , l_1 (along x direction) and l_2 (along y direction) completely define the configuration.
19 The recovered (stimuli off) and actuated (stimuli on) states are shown in Fig. 5B where widths l_r
20 (at recovered state) and l_a (at actuated state) define the device strain ε along the l_2 direction
21 according to $\varepsilon = (l_r - l_a)/l_r$. Similarly, lengths l'_r and l'_a define the device strain ε'
22 perpendicular to the l_2 direction according to $\varepsilon' = (l'_r - l'_a)/l'_r$.

23 For the light actuation, the Miura structure was illuminated by an LED light source with a
24 nominal power rating of 30 W, and a camera was used to record the motion of the structure (see
25 fig. S5A). The setup was placed in ambient laboratory conditions of 24°C temperature and 65%

1 relative humidity (RH). Figure 1B(iii) shows the natural and actuated shapes of the Miura
2 structure. When the light source was switched on to give an intensity of 120 mW/cm^2 at the Miura
3 structure, the latter contracted to a steady state in around 2 seconds (see Movie S4). As the light
4 was switched off, the Miura structure recovered to the original shape, and the process was highly
5 repeatable. The device strains ε and ε' along and perpendicular to the l_2 direction are shown in
6 Fig. 5C. The distance of the LED light from the Miura structure was varied to give different light
7 intensities at the origami actuator, which were measured by a light meter (see Materials and
8 Methods). Fig. 5D indicates that the light intensity has a profound effect on both the device strain
9 and the actuation response time of the actuator. At intensities higher than $\sim 100 \text{ mW/cm}^2$ (~ 1 sun),
10 device strains of $\sim 60\%$ can be achieved in less than 5 seconds; for example, at 150 mW/cm^2 the
11 actuation can be completed in less than 1 second (Movie S5). At illumination intensities lower
12 than ~ 1 sun, the device strain was lower, and the response was also slower. The recovery time
13 increases from 3 to 10 seconds as the light intensity increases from 30 to 150 mW/cm^2 .

14 To illustrate electrochemical actuation, a Miura fold was submerged in 1M NaOH and
15 stimulated by a step reduction potential (-0.2 V relative to Ag/AgCl electrode) to actuate, and then
16 a step oxidization potential (0.8 V relative to Ag/AgCl electrode) to recover (Movie S6). The
17 device strains along and perpendicular to the l_2 direction are also shown in Fig. 5C. The Miura
18 fold was also stimulated by a potential scan from 0.5 V (oxidized state) to -0.1 V (reduced state)
19 at a very slow scan rate of -3 mV/s to ensure quasi-equilibrium at each potential, and the device
20 strain vs potential is shown in Fig 5E. The maximum device strain ε achievable is around 60%
21 under electrochemical stimulation, which is similar to that for light stimulation. However, Fig. 5C
22 shows that the electrochemical actuation is significantly slower than the light actuation (minutes
23 vs seconds).

24 To illustrate the load lifting capability of the Miura design, a load was suspended on the
25 Miura structure along the l_2 direction. The active weight of NHO is calculated to be 47 mg, by

1 multiplying its volume (area = 5.6 cm², thickness = 2.1 μm) and density ~4.0 g/cm³ [34]. For
2 light stimulation at 120 mW/cm², a Miura can lift a weight of ~250 mg, which is a piece of
3 polymeric foam in air, with linear device strain ~0.3, as shown in Fig. 5F and Movie S7. Under
4 electrochemical stimulation by step potential -1 V applied relative to Ag/AgCl electrode in 1M
5 NaOH electrolyte, a similar Miura design can lift a load of ~120 mg, which is a piece of solid
6 plasticine (density ~1.9 g/cm³) of dry weight 250 mg before accounting for buoyancy, producing
7 linear device strain ~0.2 as shown in Fig. 5G (see Movie S8).

8

9 *3.2 Fingers with independently controlled joints in response to light and electrochemical stimuli*

10 Amongst SRM-driven origami designs published in the literature, a capability that has never
11 been reported before is independent control of different hinges in the same origami device. Here,
12 we demonstrate this capability via finger designs with independently controlled joints. These
13 fingers were fabricated using the microfluidic writing method shown in Fig. 4B, where the
14 actuation joints of either NHO or MnO_x were written on isolated conductive areas of Au
15 deposited onto the MPPC substrate. Therefore, by delivering electrochemical or light stimuli to
16 the Au areas individually, the actuation joints can be triggered independently.

17 For the electrochemical actuation, a finger-mimicking device comprising three “muscle
18 groups” I, II and III is shown in Fig. 6A. Each “muscle group” consists of several actuating strips
19 of NHO written directly onto an Au area pre-sputtered onto the MPPC substrate (see Materials
20 and Methods). The Au pattern served not only as the conductive electrode required for the
21 electrochemical writing of the NHO material, but also as the metallization needed for the
22 independent control of the muscle group on top. In Fig. 6A, each muscle group (I to III)
23 comprises two NHO strips (shown in dark gray) written onto Au domains (shown in yellow)
24 isolated from each another, supported by an underlying MPPC (shown in light gray). In the
25 subsequent actuation test (Fig. 6A, B), electrical connection with the electrochemical workstation

1 was made to the Au domains to allow the corresponding NHO muscle groups to actuate
2 independently. Under 0.8 V potential with respect to Ag/AgCl reference electrode (RE) in an
3 electrolyte of 1 M NaOH, the NHO muscle group contracted, and under 0.0 V, the muscle group
4 recovered. The bending motion of the robotic finger was captured using a camera, and markers
5 located at specific end points of the muscle groups were used for gait analysis. Fig. 6B, C and
6 Movie S9 show that the independent actuation of the muscle groups allows the finger to adopt
7 different shapes. Furthermore, to illustrate that the concept is versatile for other SRMs, MnO_x –
8 another proven SRM [23]– was printed on MPPC substrates to form electrochemical actuators.
9 The MnO_x actuating patterns exhibit good adhesion with the polymeric substrate, and also
10 demonstrate excellent actuating behavior (see fig. S4 and Movie S11). A full-hand device was
11 made from MnO_x creases on MPPC substrate, as shown in Movie S1, where the fingers can be
12 actuated independently.

13 To demonstrate independent actuation under light stimulation, another finger design
14 comprising two NHO strips (each 4 mm width) coated onto MPPC pre-sputtered uniformly with
15 Au was made. Two light sources of intensity 30 mW/cm² were used to locally stimulate the
16 actuating hinges “on demand” (Fig. 6D). The motion of the finger under four exemplary states of
17 light stimulation is shown in Fig. 6(E, F) and Movie S10.

18

19 **Discussion**

20 The critical problem of how to actuate origamis in a compact, self-contained way is solved in
21 this work by a minimalist design concept in which high-performing SRMs of transition metal
22 hydroxides/oxides are deployed to make the self-actuating creases. In particular, NHO is one of
23 the cheapest and easily made SRMs that exhibit high actuation performances under both light and
24 electrochemical stimulation, due to a change in the (001) lattice spacing or a volume-changing
25 redox reaction, respectively, as shown in the results in Fig. 2. The folding origamis are made from

1 microporous polycarbonate membranes on which actuating crease patterns are printed by
2 selective electrodeposition. The micropores on the membranes are critical in enabling the
3 formation of micro-scale rivets after growing in of the NHO material, which then provide an
4 effective means of bonding the active material layer to the substrate. The porous substrate delivers
5 much better actuating performance compared with the non-porous counterpart, demonstrating the
6 effectiveness of the micro-riveting method. Among the pore sizes of 0.03, 0.2, 3 and 10 μm
7 studied, 0.2 μm delivers the best riveting effect and 3 μm also yields comparable results (Fig. 3B);
8 therefore pore sizes ranging from 0.2 to 3 μm are optimum for device design. The smaller pores
9 of 0.03 μm exhibit relatively poor adhesion, because little NHO could be filled into the pores to
10 form strong rivets. The NHO electrodeposited on the substrate with the large pore size of 10 μm
11 also delivers relatively poor actuation performance, probably due to the larger amount of NHO
12 filled inside the passive layer, thus increasing the Young's modulus of the passive layer. Also,
13 since the formation of the NHO actuating layer is influenced by the morphology of the passive
14 layer, larger cracks can be formed inside the actuating layer, thus reducing the strength of the
15 actuating layer and its actuation performance.

16 A second SRM of MnO_x was also used in the full-hand design in Movie S1, with the same
17 micro-riveting method to achieve sufficient adhesion on MPPC substrates. The micro-riveting
18 method is therefore proven to be a rather general, versatile method deployable to different
19 ceramic-based SRMs. Apart from NHO and MnO_x , a range of other SRMs capable of changing
20 volume in response to environmental stimuli such as temperature [20, 35, 36, 37], light [20, 38,
21 39], voltage [40] or humidity [41] are in existence and may be candidate active materials for self-
22 folding creases. Future work may explore these other SRMs.

23 Another key enabling technology is the microfluidic electrochemical writing method which
24 allows arbitrary crease patterns of the active material to be written on the origami substrates. In
25 this work, we have demonstrated this method for the two SRMs of NHO and MnO_x , and it should

1 work in principle for other ceramic SRMs that can be electrodeposited by an electrochemical
2 means. Together with the more traditional bath/masked electrodeposition method, pre-designed
3 active crease patterns that can be stimulated locally and/or independently can be printed, thus
4 allowing complex shape changes. One possibility is to employ machine-learning methodologies
5 to reversely design the optimal active-crease patterns to achieve a particular category of complex
6 motions. Another interesting direction would be Miura robots with gradient or non-uniform
7 active-crease units which may also be independently stimulated. Such designs would involve
8 strained (high-energy) and unstrained (low-energy) substrate states [2], and by exploiting their
9 interplay via independently controlling the crease units, high flexibility in motion control may be
10 achieved.

11 The thickness of the present origami structures is $\sim 10\ \mu\text{m}$, which is only $\sim 0.2\ \%$ of the planar
12 dimensions of structures ($\sim 4\ \text{mm}$). Therefore, the structures can be regarded as “near-zero-
13 thickness surfaces” [42, 43]. In the Miura-fold design, the intersecting area was trimmed to reduce
14 the constraining effects of the interior vertices on the folding motion [43]. The supporting passive
15 membrane was pre-folded manually along the folding paths, which may avoid the singular
16 behavior and help the structure transform into the designed configuration smoothly during the
17 reversible folding process [44, 45]. The present fabrication methods (c.f. Fig. 4) also allow the
18 actuating SRMs to be precisely located at the actuating hinges effectively, and because of their
19 high-performing actuating performance, the origami structures could deliver large folding along
20 the folding lines. However, since a certain width of the SRM is required to achieve sufficient
21 folding along the creases, the printing method may not be suitable for micron-scale origami
22 structures. There are several degrees of complexity for folding, starting from the simple and basic
23 (mountain or valley) folding, which could be stimulated independently, to the Yoshimura units,
24 and to complex folds such as Miura-origami which contains multiple and repetitive units
25 undergoing motion “all at once” when triggered by environmental stimulations [46].

1 The multi-stimuli responsive nature of NHO enables origami structures to actuate in both
2 liquid (electrochemically stimulated) and ambient (light stimulated) environments. For the Miura
3 folds shown in Fig. 5C, under both stimuli, the eventual device strain can be up to 60 %. However,
4 the actuating strain rate under light stimulation is up to 30%/s (at intensity 120 mW/cm²), which
5 is much faster than the 0.03%/s under electrochemical actuation. For the light intensity of ~1 sun
6 (100 mW/cm²), the actuating time is up to 2 seconds, plus ~10 seconds to recover, but it will take
7 around 3.5 min for electrochemical actuation. The sluggish electrochemical actuation of the Miura
8 fold is intriguing, since for bilayered actuators comprising a uniformly coated NHO layer on
9 MPPC (Section S2, fig. S3, Movie S2) the actuation time is much shorter in a few to tens of
10 seconds. The reason for the slow actuation in the Miura case may be due to the poor conductivity
11 and the narrow widths of the NHO material in the crease pattern, and/or a stress effect on the
12 chemical kinetics of the redox reaction which drives the actuation of the NHO material. In both
13 the uniform-coating design in fig. S3 and the Miura fold in Fig. 5, the MPPC substrates had the
14 same thickness (10 μm), but in the case of the Miura fold, there is much less NHO to actuate the
15 substrate, than the uniform-coating case. The resistance stress exerted on the NHO material is
16 significantly higher in the Miura fold, so that the kinetics of the redox reaction may be suppressed.
17 Further research should investigate the mechanics effects on chemical kinetics in a systematic
18 way, for both electrochemical and light actuation.

19 Compared with electrochemical stimulation, the main advantages of light actuation in the
20 case of NHO are fast response and its wireless nature. Potential applications may include micro-
21 robots for surveillance or inspection in narrow confinements where the robot needs to travel far.
22 The main limitation or challenge is light guide technology needed to incident light specifically on
23 different actuators in a multi-actuator design. For electrochemical actuation, wiring and
24 electrolyte packaging are needed, and the response can be significantly slower. Electrochemically
25 stimulated devices are more suited for stationary applications, while independent control of

1 different parts is desirable. Examples may include prime movers in small devices, e.g. micro-fans
2 for cooling electronics, micro valves or guides in micro-fluidic channels, transducers for micro-
3 force tensile testers for soft specimens, and so on. Our technique uses inexpensive protocols and
4 reagents. It is easily adaptable and can be deployed to fabricate micro-robots for a wide range of
5 potential applications such as self-charged or integrated sensing actuating systems by combining
6 with other energy storage units [47, 48, 49, 50].

7 As stated in the Introduction, many of the SRM-driven origami designs in the past exhibited
8 slow responses requiring minutes to hours to actuate [13, 14, 15] (Table S1). Liquid-crystal
9 elastomers show fast responses in seconds [17], but these materials require heat-light coupled pre-
10 programming, and the actuation is triggered by temperature changes which are less convenient to
11 deliver in a compact design, or one in which multiple actuators need to be controlled
12 independently. Graphene oxide which exhibits fast actuation responses in seconds [20] under light,
13 heat or humidity stimuli will be a good SRM for making actuating creases, but the fabrication is
14 complicated (sonication for 100 min, stirring for 12 h, centrifugation, washing, filtration, etc.) and
15 it requires near infrared (NIR) light to actuate. Also, these SRMs may not be easily integrated [15,
16 20] to make intersecting mountain and valley hinges, and therefore a lot of complex origami
17 structures with high application potential such as Miura-ori and waterbomb may not be achievable
18 [51]. The present transition metal hydroxide/oxide-based SRMs may be more promising in terms
19 of their multi-stimuli response to both voltage and visible light signals, which are easier to deliver
20 and control than heat or humidity changes. They are also fast responding in seconds, and easy and
21 cheap to fabricate. Table S1 summarizes the comparison of various SRMs with the ones studied
22 in this work.

23

24 **Conclusion**

1 A new concept for origami robotics was demonstrated to actuate micro-robots by stimuli-
2 responsive hinges made of a type of actuating hydroxides/oxides supported on micro-porous
3 polymer substrates. Combining the methods of micro riveting and microfluidic electrochemical
4 writing of the stimuli-responsive hydroxides/oxides, a versatile yet simple paradigm for
5 fabricating micro-robots with fast response and independently controllable degrees of freedom of
6 motion was established. The fabricated stimuli-responsive hinges can be stimulated by visible
7 light of intensities less than 1 sun in ambient conditions, or electrochemical potential of less than
8 1 V in alkaline electrolytes, to perform reversible shape transformation as fast as in seconds.
9 Based on such self-folding hinges, complex origamis including Miura folds and a micro-robotic
10 hand with independently controllable finger hinges were achieved. The present approach is
11 versatile for different stimuli-responsive materials that can be electrodeposited, and is easily
12 adaptable for the fabrication of compact micro-robots with multi-stimulated, controllable,
13 reversible and fast shape transformation.

14 **Materials and Methods**

15 Nuclepore Track-Etched Polycarbonate Membranes with a diameter of 47 mm and a pore size of
16 0.03, 0.2, 3 and 10 μm (MPPC membranes) were purchased from Whatman[®]. Non-porous
17 polycarbonate (PC) membrane of 6 μm thick was purchased from Goodfellow. Nickel sulfate
18 heptahydrate ($\text{NiSO}_4 \cdot 7\text{H}_2\text{O}$), manganese (II) acetate tetrahydrate ($\text{C}_4\text{H}_6\text{MnO}_4 \cdot 4\text{H}_2\text{O}$) in purum p.a.
19 grade, sodium acetate (CH_3COONa), sodium sulfate (Na_2SO_4), sodium sulfite (Na_2SO_3) in puriss.
20 p.a. grade, and sodium hydroxide (NaOH) in reagent grade, were purchased from Sigma–Aldrich
21 and used as received. An electroless Au-plating solution (Oromerse SO Part B) was obtained from
22 Technic Inc for the Au electrodeposition. Copper (Cu) tape was purchased from 3M. Deionized
23 (DI) water with a resistivity of ~ 18 megohms·cm was utilized to make solution baths and for
24 rinsing.
25

26 **Bath electrodeposition of NHO on MPPC membranes**

1 Actuating material NHO was electrodeposited on MPPC membranes using an electrochemical
2 workstation (LK2006A, Lanlike) in a beaker-type electrochemical cell equipped with a working
3 electrode, a platinum mesh counter electrode, and a saturated calomel reference electrode. To
4 metallize the MPPC membranes for the electrodeposition, they were first sputtered with a uniform
5 thin layer of Au of 14 nm thick, in a Bal-tec SCD 005 Sputter Coater (working distance: 50 mm,
6 sputtering current: 30 mA, sputtering duration: 100 s). The Au-sputtered MPPC membranes were
7 then used as the working electrodes in the electrodeposition process. The electrodepositing bath
8 solution was 0.13 M NiSO₄, 0.13 M CH₃COONa and 0.1 M of Na₂SO₄ [21]. An anodic current
9 density of 1.2 mA/cm² for durations from 0.5 h to 2.5 h was applied under continuous and
10 vigorous stirring, and this resulted in a layered film comprising a dark, uniform layer of NHO on
11 top of the Au-sputtered MPPC membrane. The as-deposited NHO made using this protocol was in
12 the oxidized state, with an XRD profile shown as the black curves in Fig. 2B(a,b).

13 To fabricate folding structures with active crease patterns as shown in Figs. 4 and 5, a pre-
14 designed Au pattern instead of a uniform layer had to be sputtered on the MPPC membranes. For
15 the Miura and Yoshimura patterns shown in Fig. 5 and fig. S5, the corresponding Au patterns
16 were achieved by placing inverse masks on top of the membranes before Au sputtering. The
17 masks were designed by AutoCAD and fabricated by laser cutting acrylic plastic sheets of 2 mm
18 thick. Crease patterns of NHO could then be electrodeposited on the membranes as shown in Fig.
19 4A(b), by the above bath electrodeposition protocol for 2 h. For the electrochemically stimulated
20 Miura folds, to further increase the adhesion between NHO and the Au-sputtered membrane, an
21 extra Au layer was electrodeposited on the Au-sputtered membrane before NHO
22 electrodeposition. The Au electrodepositing bath solution was Oromerse SO Part B and 1.7M
23 Na₂SO₃ with the volume ratio of 1:9. A cathodic current density of -0.1 mA/cm² for a duration of
24 30 min was applied without stirring, and this resulted in a uniform Au layer. The finger design
25 comprising two actuating hinges for independent light stimulation in Fig. 6D and F was also

1 fabricated by inverse masks to leave two unpainted rectangular windows of 4 mm width by 8 mm
2 length, which were then electrodeposited with NHO using an applied current density of 1.2
3 mA/cm² for 2 h.

4 For the Miura structure shown in Fig. 4A and 5, after the electrodeposition of the NHO crease
5 pattern, the MPPC membrane was folded along the sharp creases manually to allow the device to
6 actuate in the intended way when stimulated by light. To make the individual actuating creases
7 shown in Fig. 1B(i), designated areas of the Au-sputtered MPPC membranes (8 mm width by 16
8 mm length) were painted with a marker pen to leave an unpainted rectangular area of 4 mm width
9 by 8 mm length, onto which NHO was coated by subsequent bath-electrodeposition with an
10 applied current density of 1.2 mA/cm² for 2 h.

11 The actuation characterization tests shown in figs. S2 and S3 were performed on cantilever
12 actuators with NHO electrodeposited by the above bath electrodeposition protocol on uniformly
13 Au-sputtered MPPC membranes. Part of the Au was adhered to Cu tape for electrical connection
14 to the electrochemical workstation. The just fabricated actuators were cut into rectangular strips
15 measuring approximately 15 mm by 3 mm to form the cantilever actuators.

16

17 **Electrodeposition of Ni(OH)₂/NiOOH (NHO) and MnO_x patterns on micro-porous** 18 **polycarbonate (MPPC) membranes by microfluidic electrochemical writing**

19 In the electrochemically triggered micro-finger shown in Fig. 6A to C, muscle groups of the NHO
20 material were printed onto isolated Au areas, which were then individually connected to the
21 workstation electrodes. To start with, the conductive Au areas were patterned by sputtering MPPC
22 membranes covered with acrylic masks. Then, NHO was directly written onto the sputtered Au
23 areas by the microfluidic electrochemical writing method discussed in Section 2.2, in which the
24 required electrolyte was delivered locally by micro-fluidic means [33] (Figs. 1C(i) and 4B). An
25 electrolyte containing 0.6 M NiSO₄, 0.53 M CH₃COONa and 0.1 M of Na₂SO₄ was put into the

1 syringe of the setup which has a capacity of 3 mL. The NHO was electrodeposited under a
2 constant potential of 2.05 V applied to the Au areas of the membrane against the stainless-steel
3 syringe needle. The inner diameter of the needle was 0.51 mm, and the printing was performed by
4 moving the syringe needle at a speed of 50 mm/min. To achieve thicker active layers of NHO, the
5 writing was conducted by repeatedly scanning over the same area for a total duration of 20 min.
6 Each actuating layer measured 10 mm in length and was printed parallel to the folding hinge.

7 For the MnO_x printing, active MnO_x hinges were electrodeposited on Au sputtered areas pre-
8 patterned by reversed acrylic masks. The MnO_x printing electrolyte was a mixture of 0.1 M
9 C₄H₆MnO₄·4H₂O and 0.1 M Na₂SO₄ [52]. The constant potential and needle speed used for the
10 writing were 2.3 V and 0.5 mm/min, respectively. The single curling actuator shown in fig.
11 S4B was 5 mm wide, and it comprised eight parallel MnO_x actuating strips. Each actuating strip
12 measured 5 mm in length and 1 mm in width, and was separated 2 mm apart. For the full micro-
13 robotic hand shown in fig. S4A and Movie S1, each MnO_x active strip was 5 mm long and was
14 printed for a total duration of 10 min.

15

16 **Physical characterization**

17 Scanning electron microscope (SEM) images were obtained with a LEO 1530 field-emission
18 microscope to image the surface morphology and thickness of NHO. The thickness of the MPPC
19 membranes was measured by Bruker DektakXT® stylus profiler. Microstructural characterization
20 was carried out by in-plane grazing incidence X-ray diffraction (GIXRD). In-plane GIXRD was
21 performed in a Rigaku SmartLab diffractometer with a fixed incidence angle of 0.5° using a
22 monochromatic Cu K-alpha source (wavelength = 1.54 Å) with the scan rate being 1°/min at steps
23 of 0.1°. For *in situ* XRD measurements, a lower scan rate of 0.05°/min was used. Transmission
24 electron microscopy (TEM) imaging and selected area electron diffraction (SAED) were

1 performed in a FEI Tecnai G2 20 Scanning TEM. The Young's moduli of MPPC and NHO were
2 measured by nanoindentation (Agilent Nano Indenter G200).

3 **Light stimulated actuation tests**

4 The light stimulated origami tests were performed with the NHO in the as-fabricated, oxidized
5 state at ambient conditions in the laboratory, with temperature and RH being 24°C and 65%,
6 respectively. An LED light source of nominal power rating of 30 W was utilized to trigger the
7 actuation as shown in fig. S5A. By modifying the distance between the light source and the
8 illuminated targeted area, the light intensities at the latter were varied from 30 to 150 mW/cm², as
9 measured by a TES11333 solar power meter (TES Electrical electronic Corp.). The Miura lift was
10 stimulated at light intensity ~120 mW/cm², with a load ~250 mg. For the independently controlled
11 tests under light stimulation (Fig. 6D), two light sources combined with optical fibers were used
12 to stimulate the actuating hinges. The light intensity at the hinges was around 30 mW/cm², as
13 measured by a solar power meter.

14

15 **Electro-chemical actuation tests**

16 The electrochemical actuation tests in Figs. 1B, 3, 5 and 6 were carried out with the NHO in the
17 as-fabricated, oxidized state, and the actuators were submerged into an electrolyte of 1 M NaOH
18 solution in a rectangular glass container. One end of the actuator was fixed and connected to an
19 electrochemical workstation (LK2006A, Lanlike or Corrtest, CS350) as the working electrode. In
20 Fig 3 and figs. S2 and S3, the actuation was electrochemically induced by the cyclic voltammetry
21 mode of the workstation from 0 V to 0.8 V with respect to an Ag/AgCl reference electrode in a 3-
22 electrode cell setup with a platinum mesh counter electrode. The actuation motion was video-
23 recorded and was further processed and analyzed by a motion tracking software Kinovea. The
24 actuation performance of the printed fingers was characterized by fixing them vertically in the
25 same three-electrode setup (Fig. 6A). Each muscle group was connected to a toggle switch which

1 enabled the actuator to switch between input voltage of 0.0 V and 0.8 V. For the Miura device,
2 the freshly prepared actuator was fixed in 1M NaOH solution, with the reduced potential (-0.2 V)
3 to actuate the Miura fold and oxidized potential (0.8 V) to recover it. Also, the actuator was
4 stimulated by the potential window -0.1 V to 0.5 V with a scan rate of 3 mV/s to demonstrate the
5 actuating performance vs varying potentials in quasi-equilibrium conditions. The Miura lift was
6 stimulated by a step potential (-1 V) to lift a load ~120 mg in the 1M NaOH solution, where
7 buoyancy was calculated as volume of the load times its density. The printed MnO_x curling
8 actuator and the full hand were submerged in an electrolyte of 0.5 M Na₂SO₄ electrolyte in a
9 rectangular glass container. The curling actuator was connected to a multiple toggle switch,
10 enabling the input voltage to switch between different step potentials (see Section S2). For the
11 printed MnO_x full hand, each finger was independently connected to a toggle switch, enabling the
12 input voltage to switch between 0.0 and 1.0 V [23] relative to Ag/AgCl electrode, to actuate and
13 recover each finger independently.

14 **Data availability**

15 All data needed to support the conclusions of this manuscript are included in the main text or the
16 Supplementary Materials.

18 **References and Notes**

- 20 [1] D. Rus, M. T. Tolley, Design, fabrication and control of origami robots, *Nat. Rev. Mater.* **3**
21 (2018) 101–112. <https://doi.org/10.1038/s41578-018-0009-8>.
- 22 [2] M. B. Pinson, M. Stern, A. C. Ferrero, T. A. Witten, E. Chen, A. Murugan, Self-folding
23 origami at any energy scale, *Nat. Commun.* **8** (2017) 15477.
24 <https://doi.org/10.1038/ncomms15477>.
- 25 [3] D. Rus, C. Sung, Spotlight on origami robots, *Sci. Robot.* **3** (2018) eaat0938.
26 <https://doi.org/10.1126/science.1252610>.

- 1 [4] P. Sareh, P. Chermprayong, M. Emmanuelli, H. Nadeem, M. Kovac, Rotorigami: A rotary
2 origami protective system for robotic rotorcraft, *Sci. Robot.* **3** (2018) eaah5228.
3 <https://doi.org/10.1126/scirobotics.aah5228>.
- 4 [5] E. D. Demaine, J. O'Rourke, *Geometric folding algorithms: Linkages, origami, polyhedra*,
5 Camb. Univ. Press, 2007. <https://doi.org/10.1017/CBO9780511735172.001>
- 6 [6] Y. Chen, P. Sareh, J. Yan, A. S. Fallah, J. Feng, An integrated geometric-graph-theoretic
7 approach to representing origami structures and their corresponding truss frameworks, *J.*
8 *Mech. Des.* **141** (2019) 091402. <https://doi.org/10.1115/1.4042791>.
- 9 [7] S. Felton, M. Tolley, E. Demaine, D. Rus, R. Wood, A method for building self-folding
10 machines, *Science* **345** (2014) 644–646. <https://doi.org/10.1126/science.1252610>.
- 11 [8] R. V. Martinez, C. R. Fish, X. Chen, G. M. Whitesides, Elastomeric Origami : Programmable
12 Paper-Elastomer Composites as Pneumatic Actuators, *Adv. Funct. Mater.* **22** (2012) 1376–
13 1384. <https://doi.org/10.1002/adfm.201102978>.
- 14 [9] S. Li, D. M. Vogt, D. Rus, R. J. Wood, Fluid-driven origami-inspired artificial muscles, *Proc.*
15 *Natl. Acad. Sci.* **114** (2017) 13132–13137. <https://doi.org/10.1073/pnas.1713450114>.
- 16 [10] S. Miyashita, S. Guitron, M. Ludersdorfer, C. R. Sung, D. Rus, An untethered miniature
17 origami robot that self-folds, walks, swims, and degrades, *IEEE Int. Conf. Robot. Autom.*
18 (2016) 1490–1496. <https://doi.org/10.1109/ICRA.2015.7139386>.
- 19 [11] Y. Kim, H. Yuk, R. Zhao, S. A. Chester, X. Zhao, Printing ferromagnetic domains for
20 untethered fast-transforming soft materials, *Nature* **558** (2018) 274–279.
21 <https://doi.org/10.1038/s41586-018-0185-0>.
- 22 [12] C. De Marco, S. Pané, B. J. Nelson, 4D printing and robotics, *Sci. Robot.* **3** (2018) eaau0449.
23 <https://doi.org/10.1126/scirobotics.aau0449>.

- 1 [13]Z. Zhao, J. Wu, X. Mu, H. Chen, H. J. Qi, D. Fang, Desolvation induced origami of
2 photocurable polymers by digit light processing, *Macromol. Rapid Comm.* **38** (2017)
3 1600625. <https://doi.org/10.1002/marc.201600625>.
- 4 [14]Y. Mao, Z. Ding, C. Yuan, S. Ai, M. Isakov, J. Wu, T. Wang, M. L. Dunn, H. J. Qi, 3D
5 printed reversible shape changing components with stimuli responsive materials, *Sci. Rep.* **6**
6 (2016) 24761. <https://doi.org/10.1038/srep24761>.
- 7 [15]B. Jin, H. Song, R. Jiang, J. Song, Q. Zhao, T. Xie, Programming a crystalline shape memory
8 polymer network with thermo-and photo-reversible bonds toward a single-component soft
9 robot, *Sci. Adv.* **4** (2018) eaao3865. <https://doi.org/10.1126/sciadv.aao3865>.
- 10 [16]J. H. Na, A. A. Evans, J. Bae, M. C. Chiappelli, C. D. Santangelo, R. J. Lang, T. C. Hull, R.
11 C. Hayward, Programming reversibly self-folding origami with micropatterned
12 photo-crosslinkable polymer trilayers, *Adv. Mater.* **27** (2015) 79–85.
13 <https://doi.org/10.1002/adma.201403510>.
- 14 [17]M. K. McBride, A. M. Martinez, L. Cox, M. Alim, K. Childress, M. Beiswinger, M.
15 Podgorski, B. T. Worrell, J. Killgore, C. N. Bowman. A readily programmable, fully
16 reversible shape-switching material, *Sci. Adv.* **4** (2018) eaat4634.
17 <https://doi.org/10.1126/sciadv.aat4634>.
- 18 [18]Q. Ge, C. K. Dunn, H. J. Qi, M. L. Dunn, Active origami by 4D printing, *Smart. Mater.*
19 *Struct.* **23** (2014) 094007. <https://doi.org/10.1088/0964-1726/23/9/094007>.
- 20 [19]H. Shigemune, S. Maeda, Y. Hara, N. Hosoya, S. Hashimoto, Origami robot: A self-folding
21 paper robot with an electrothermal actuator created by printing, *IEEE-ASME T. Mech.* **21**
22 (2016) 2746–2754. <https://doi.org/10.1109/TMECH.2016.2593912>.
- 23 [20]J. Mu, C. Hou, H. Wang, Y. Li, Q. Zhang, M. Zhu, Origami-inspired active graphene-based
24 paper for programmable instant self-folding walking devices, *Sci. Adv.* **1** (2015) e1500533.
25 <https://doi.org/10.1126/sciadv.1500533>.

- 1 [21]K. W. Kwan, N. Y. Hau, S. P. Feng, A. H. W. Ngan, Electrochemical actuation of nickel
2 hydroxide/oxyhydroxide at sub-volt voltages, *Sensor. Actuat. B-Chem.* **248** (2017) 657–664.
3 <https://doi.org/10.1016/j.snb.2017.04.009>.
- 4 [22]K. W. Kwan, S. J. Li, N. Y. Hau, W. D. Li, S. P. Feng, A. H. W. Ngan, Light-stimulated
5 actuators based on nickel hydroxide-oxyhydroxide, *Sci. Robot.* **3** (2018) eaat4051.
6 <https://doi.org/10.1126/scirobotics.aat4051>.
- 7 [23]L. Liu, L. Su, Y. Lu, Q. Zhang, L. Zhang, S. Lei, S. Shi, M. D. Levi, X. Yan, The Origin of
8 electrochemical actuation of MnO₂/Ni bilayer film derived by redox pseudocapacitive process,
9 *Adv. Funct. Mater.* **29** (2019) 1806778. <https://doi.org/10.1002/adfm.201806778>.
- 10 [24]M. Agarwala, D. Bourell, J. Beaman, H. Marcus, J. Barlow, Direct selective laser sintering of
11 metals, *Rapid. Prototyping J.* **1** (1995) 26–36. <https://doi.org/10.1108/13552549510078113>.
- 12 [25]B. Derby, N. Reis, Inkjet printing of highly loaded particulate suspensions, *MRS Bull.* **28**
13 (2013) 815–818. <https://doi.org/10.1557/mrs2003.230>.
- 14 [26]K. Nagase, S. Kubo, M. Nakagawa, Photochemically grafted polystyrene layer assisting
15 selective Au electrodeposition, *Langmuir* **28** (2012) 11646–11653.
16 <https://doi.org/10.1021/la301632y>.
- 17 [27]S. H. Cho, S. H. Kim, J. G. Lee, N. E. Lee, Micro-scale metallization of high aspect-ratio Cu
18 and Au lines on flexible polyimide substrate by electroplating using SU-8 photoresist mask,
19 *Microelectron. Eng.* **77** (2005) 116–124. <https://doi.org/10.1016/j.mee.2004.09.007>.
- 20 [28]D. S. Hall, D. J. Lockwood, C. Bock, B. R. MacDougall, Nickel hydroxides and related
21 materials: a review of their structures, synthesis and properties, *Proc. Math. Phys. Eng. Sci.*
22 **471** (2015) 20140792. <https://doi.org/10.1098/rspa.2014.0792>.
- 23 [29]C. Faure, C. Delmas, M. Fouassier, Characterization of a turbostratic α -nickel hydroxide
24 quantitatively obtained from an NiSO₄ solution, *J. Power Sources* **35** (1991) 279–290.
25 [https://doi.org/10.1016/0378-7753\(91\)80112-B](https://doi.org/10.1016/0378-7753(91)80112-B).

- 1 [30]K. W. Kwan, D. G. Xie, R. R. Zhang, Z. W. Shan, A. H. W. Ngan, Electron - beam induced
2 water removal, phase change, and crystallization of anodic - electrodeposited turbostratic
3 nickel hydroxide-oxyhydroxide, *Phys. Status Solidi A*. **215** (2018) 1800623.
4 <https://doi.org/10.1002/pssa.201800623>.
- 5 [31]S. Timoshenko, Analysis of bi-metal thermostats, *J. Optical. Soc. Am.* **11** (1925) 233–255.
6 <https://doi.org/10.1364/JOSA.11.000233>.
- 7 [32]J. D. Madden, N. Vandesteeg, P. A. Anquetil, P. G. Madden, A. Takshi, R. Z. Pytel, S. R.
8 Lafontaine, P. A. Wieringa, I. W. Hunter, Artificial muscle technology: physical principles
9 and naval prospects, *IEEE J. Oceanic. Eng.* **29** (2004) 706–728.
10 <https://doi.org/10.1109/JOE.2004.833135>.
- 11 [33]P. Wang, R. C. Roberts, A. H. W. Ngan, Direct microfabrication of oxide patterns by local
12 electrodeposition of precisely positioned electrolyte: The case of Cu₂O, *Sci. Rep.* **6** (2016)
13 27423. <https://doi.org/10.1038/srep27423>.
- 14 [34]Q. Xu, T. Kobayashi, *Advanced Materials for Clean Energy*, first ed., CRC Press, 2015.
15 <https://doi.org/10.1201/b18287>.
- 16 [35]L. T. de Haan, V. Gimenez-Pinto, A. Konya, T. S. Nguyen, J. M. N. Verjans, C.
17 Sánchez-Somolinos, J. V. Selinger, R. L. B. Selinger, D. J. Broer, A. P. H. J. Schenning,
18 Accordion-like actuators of multiple 3D patterned liquid crystal polymer films, *Adv. Funct.*
19 *Mater.* **24** (2014) 1251–1258. <https://doi.org/10.1002/adfm.201302568>.
- 20 [36]J. Mu, M. J. Andrade, S. Fang, X. Wang, E. Gao, N. Li, S. H. Kim, H. Wang, C. Hou, Q.
21 Zhang, M. Zhu, D. Qian, H. Lu, D. Kongahage, S. Talebian, J. Foroughi, G. Spinks, H. Kim,
22 T. H. Ware, H. J. Sim, D. Y. Lee, Y. Jang, S. J. Kim, R. H. Baughman, Sheath-run artificial
23 muscles, *Science* **365** (2019) 150-155. <https://doi.org/10.1126/science.aaw2403>.

- 1 [37]M. Kanik, S. Orguc, G. Varnavides, J. Kim, T. Benavides, D. Gonzalez, T. Akintilo, C. C.
2 Tasan, A. P. Chandrakasan, Y. Fink, P. Anikeeva, Strain-programmable fiber-based artificial
3 muscle, *Science* **365** (2019) 145-150. <https://doi.org/10.1126/science.aaw2502>.
- 4 [38]S. Kobatake, S. Takami, H. Muto, T. Ishikawa, M. Irie, Rapid and reversible shape changes
5 of molecular crystals on photoirradiation, *Nature* **446** (2007) 778–781.
6 <https://doi.org/10.1038/nature05669>.
- 7 [39]Y. Hu, G. Wu, T. Lan, J. J. Zhao, Y. Liu, W. Chen, A graphene-based bimorph structure for
8 design of high performance photoactuators, *Adv. Mater.* **27** (2015) 7867–7873.
9 <https://doi.org/10.1002/adma.201502777>.
- 10 [40]M. Acerce, E. K. Akdoğan, M. Chhowalla, Metallic molybdenum disulfide nanosheet-based
11 electrochemical actuators, *Nature* **549** (2017) 370–373. <https://doi.org/10.1038/nature23668>.
- 12 [41]H. Arazoe, D. Miyajima, K. Akaike, F. Araoka, E. Sato, T. Hikima, M. Kawamoto, T. Aida,
13 An autonomous actuator driven by fluctuations in ambient humidity, *Nat. Mater.* **15** (2016)
14 1084–1089. <https://doi.org/10.1038/nmat4693>.
- 15 [42]Y. Chen, R. Peng, Z. You, Origami of thick panels, *Science* **349** (2015) 396–400.
16 <https://doi.org/10.1126/science.aab2870>.
- 17 [43]T. Tachi, Rigid-foldable thick origami, *Origami 5: Fifth Int. Meet. Origami Sci. Math. Educ.*
18 (2011) 253-264. <https://doi.org/10.1201/b10971-24>.
- 19 [44]Y. Chen, J. Feng, Q. Sun, Lower-order symmetric mechanism modes and bifurcation behavior
20 of deployable bar structures with cyclic symmetry, *Int. J. Solids Struct.* **139** (2018) 1–14.
21 <https://doi.org/10.1016/j.ijsolstr.2017.05.008>.
- 22 [45]E. T. Filipov, K. Liu, T. Tachi, M. Schenk, G. H. Paulino, Bar and hinge models for scalable
23 analysis of origami, *Int. J. Solids Struct.* **124** (2017) 26–45.
24 <https://doi.org/10.1016/j.ijsolstr.2017.05.028>.

- 1 [46]Y. Chen, J. Yan, J. Feng, Geometric and Kinematic Analyses and Novel Characteristics of
2 Origami-Inspired Structures, *Symmetry*, **11**, (2019), 1101.
3 <https://doi.org/10.3390/sym11091101>
- 4 [47]H. Li, C. Zhao, X. Wang, J. Meng, Y. Zou, S. Noreen, L. Zhao, Z. Liu, H. Ouyang, P. Tan,
5 M. Yu, Y. Fan, Z. L. Wang, Z. Li. Fully bioabsorbable capacitor as an energy storage unit for
6 implantable medical electronics, *Adv. Sci.* **6** (2019) 1801625.
7 <https://doi.org/10.1002/advs.201970035>.
- 8 [48]J. Sun, A. Yang, C. Zhao, F. Liu, Z. Li, Recent progress of nanogenerators acting as
9 biomedical sensors in vivo, *Sci. Bull.* **64** (2019) 1336–1347.
10 <https://doi.org/10.1016/j.scib.2019.07.001>.
- 11 [49]Y. Zou, P. Tan, B. Shi, H. Ouyang, D. Jiang, Z. Liu, H. Li, M. Yu, C. Wang, X. Qu, L. Zhao,
12 Y. Fan, Z. L. Wang, Z. Li. A bionic stretchable nanogenerator for underwater sensing and
13 energy harvesting, *Nat. commun.* **10** (2019) 2695.
14 <https://doi.org/10.1038/s41467-019-10433-4>.
- 15 [50]D. Jiang, B. Shi, H. Ouyang, Y. Fan, Z. L. Wang, Z. M. Chen, Z. Li, A 25-year bibliometric
16 study of implantable energy harvesters and self-powered implantable medical electronics
17 researches, *Mater. Today Energy* **16** (2020) 100386.
18 <https://doi.org/10.1016/j.mtener.2020.100386>
- 19 [51]N. Turner, B. Goodwine, M. Sen, A review of origami applications in mechanical
20 engineering, *Proc. Inst. Mech. Eng. C* **230** (2016) 2345–2362.
21 <https://doi.org/10.1177/0954406215597713>.
- 22 [52]D. Tench, L. F. Warren, Electrodeposition of conducting transition metal oxide/hydroxide
23 films from aqueous solution, *J. Electrochem. Soc.* **130** (1983) 869-872.
24 <https://doi.org/10.1149/1.2119838>.

1 [53]Q. M. Zhang, V. V. Bharti, X. Zhao, Giant electrostriction and relaxor ferroelectric behavior
2 in electron-irradiated poly (vinylidene fluoride-trifluoroethylene) copolymer, Science **280**
3 (1998) 2101–2104. <https://doi.org/10.1126/science.280.5372.2101>.

4 [54]H. J. Jin, X. L. Wang, S. Parida, K. Wang, M. Seo, J. Weissmüller, Nanoporous Au– Pt
5 alloys as large strain electrochemical actuators, Nano lett. **10** (2009) 187–194.
6 <https://doi.org/10.1021/nl903262b>.

7 [55] J. Mcbreen, in: C. Daniel, J. O. Besenhard (Eds.), Nickel Hydroxide, in Handbook of Battery
8 Materials, Wiley-VCH Verlag, 2011. <https://doi.org/10.1002/9783527637188.ch5>

9 **Acknowledgments**

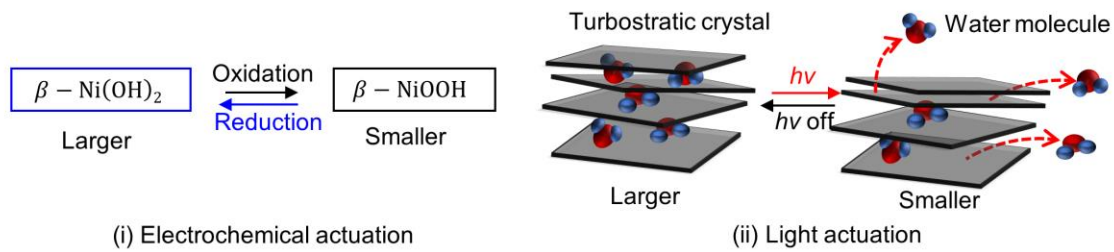
10 **General:** We thank Mr F.Y.F. Chan for help with TEM sample preparation and TEM operation.

11 **Funding:** The work is funded by the Kingboard Endowed Professorship in Materials Engineering
12 at the University of Hong Kong. **Author contributions:** All authors conceived the idea and
13 designed the experiments. A.H.W.N. supervised the overall research. K.W.K. and R.W.
14 developed the micro-riveting method. A.H.W.N and R.W. designed the Miura structure.
15 A.H.W.N. and P.W. designed the microfluidic electrochemical writing method and P.W., K.W.K.,
16 R.W. and W.M. developed it for printing NHO and MnO_x. R.W. performed actuator fabrication,
17 actuation experiments, materials characterization and collected the data. R.W., K.W.K. and
18 A.H.W.N. derived the mathematical model, did the analysis and wrote the paper. All authors have
19 given approval to the final version of the manuscript. **Competing interests:** The authors declare
20 that they have no competing interests.
21

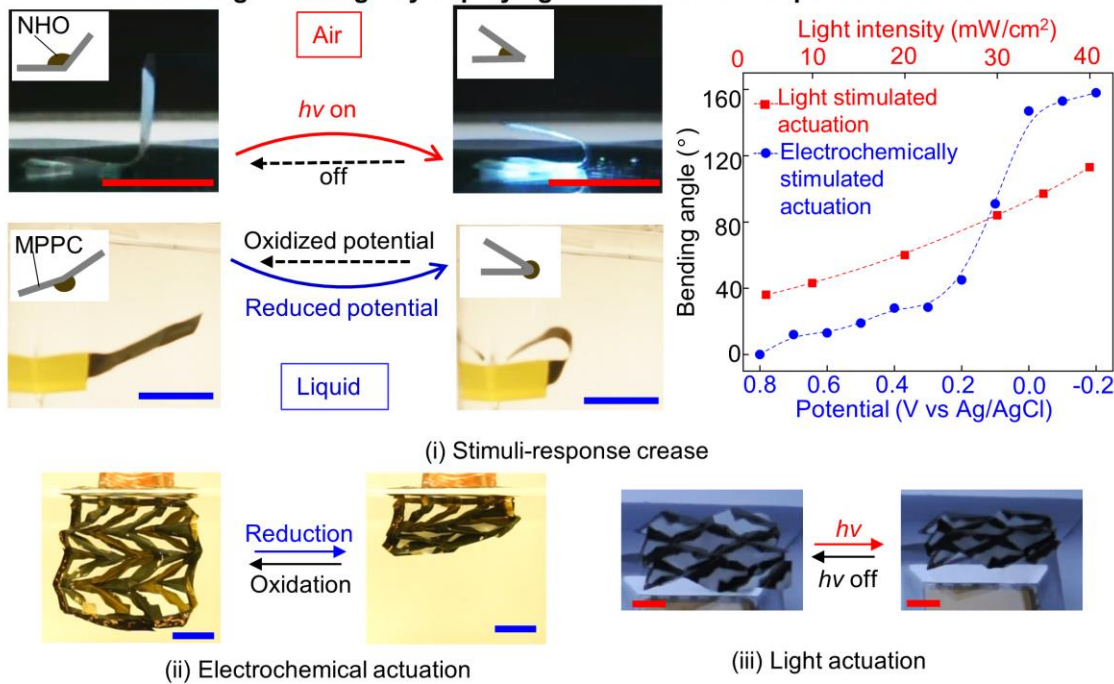
1 **Figures and Tables**

2

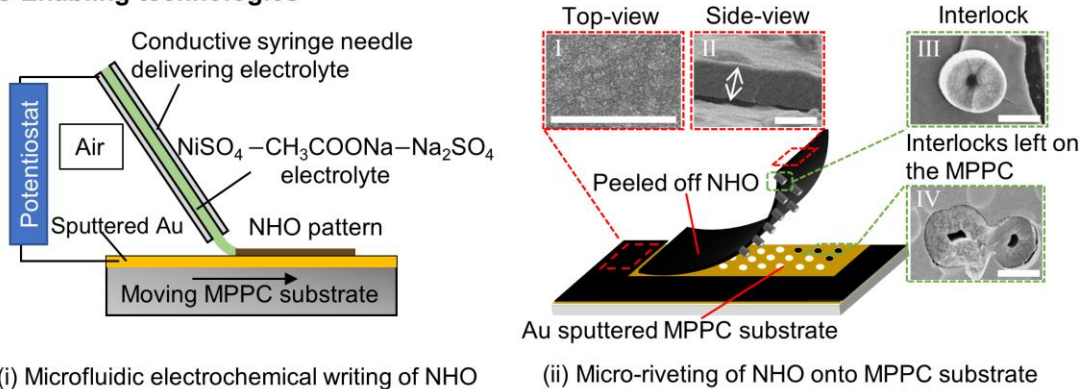
A Ni(OH)₂/NiOOH actuating material (NHO)



B “Minimalist” Origami design by deploying NHO as stimuli-response creases



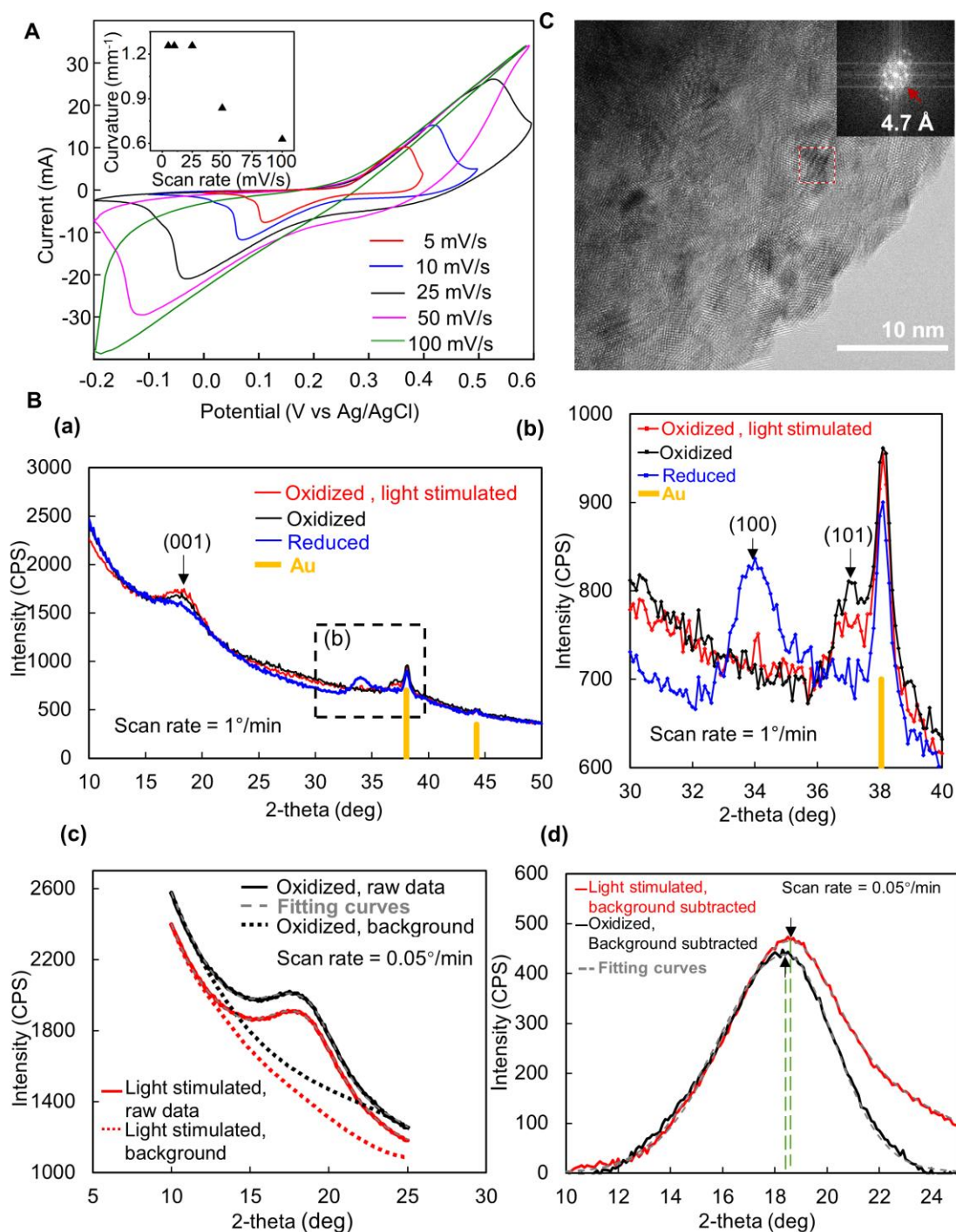
C Enabling technologies



3
4

5 **Fig. 1. “Minimalist” origami with stimuli-responsive creases. (A)** The Ni(OH)₂/NiOOH (NHO)
6 material mixture exhibits reversible volume shrinkage on (i) oxidation, or (ii) upon visible light
7 illumination. **(B)** (i) Stimuli-responsive crease made by coating a 4mm-wide NHO strip (black)

1 onto micro-porous polycarbonate (MPPC) substrate (gray), under visible light stimuli of different
2 intensities, and electrochemical stimuli at potential scan rate 25 mV/s relative to Ag/AgCl
3 electrode in 1M NaOH electrolyte (see Movie S3). (ii, iii) Typical self-actuating Miura origamis
4 with NHO crease patterns (dark colored) on MPPC membrane (gray colored) as origami substrate,
5 under (ii) electrochemical actuation in 1M NaOH, and (iii) visible light actuation at intensity of
6 120 mW/cm². Scale bar: 10 mm. See Movie S3. (C) Enabling technologies to apply NHO to
7 make self-folding origami creases: (i) microfluidic electrochemical writing of NHO onto origami
8 substrate, and (ii) micro-riveting NHO onto MPPC membrane which serves as origami substrate.
9 Insets in (ii) show SEM images of the (I) surface morphology and (II) cross-section view of NHO,
10 and (III, IV) micro-rivets formed during electrodeposition. Scale bar: 2 μm.



1

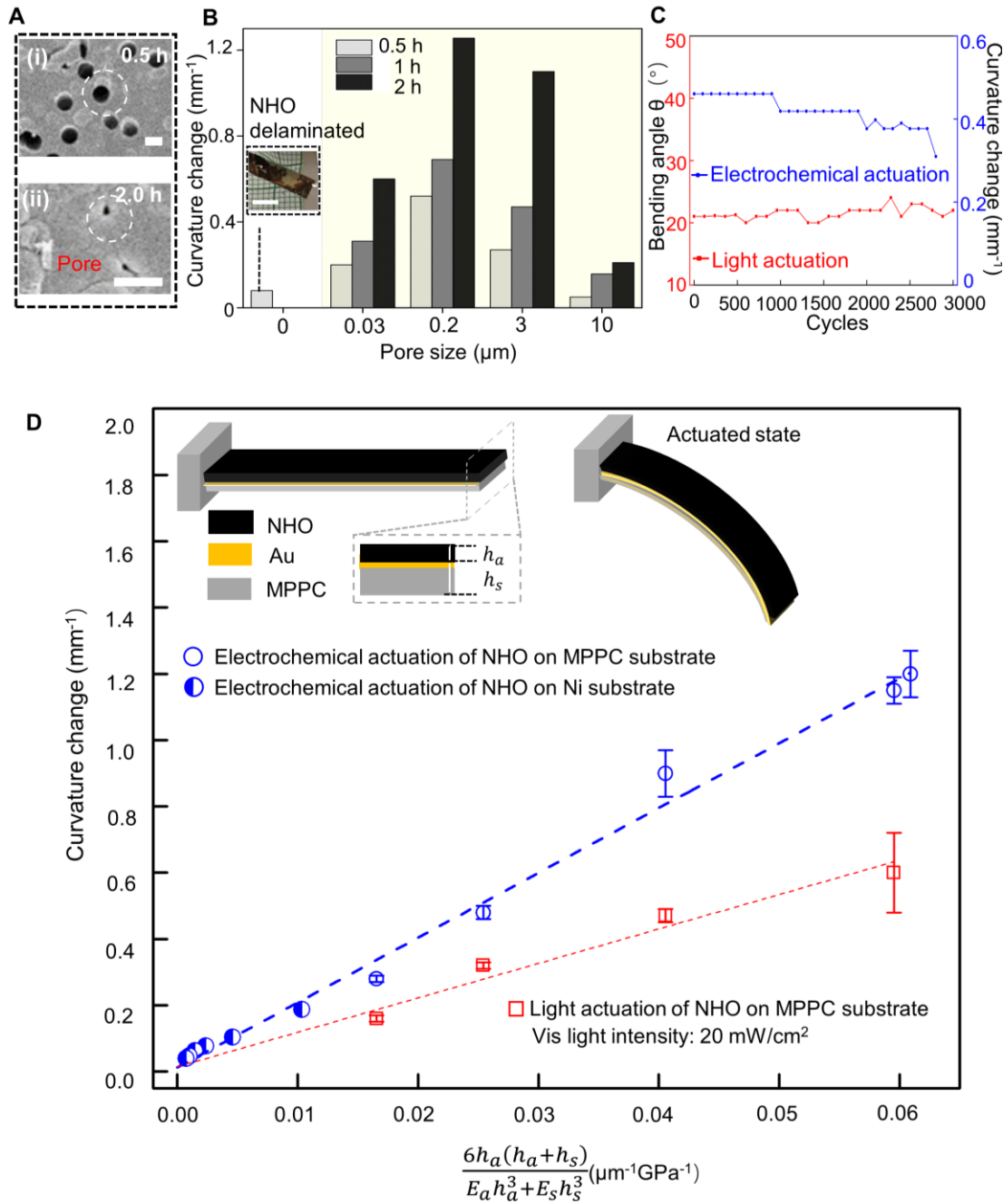
2 **Fig. 2. Stimuli-responsive microstructural changes in NHO.** (A) Cyclic voltammogram of

3 NHO in 1 M NaOH at different scan rates; inset shows curvature at different scan rates. (B) (a) *In*

4 *situ* GIXRD results of NHO under light stimulated oxidized (red), oxidized (black), and reduced

5 (blue) states at scan rate of $1^\circ/\text{min}$. (b) Enlarged view of (a). (c) *In situ* GIXRD results of NHO

- under light stimulated oxidized (red) and oxidized (black) at slower scan rate of $0.05^\circ/\text{min}$. (d)
- Background subtracted XRD spectra of (c). (C) HRTEM micrograph of oxidized NHO.



3

4 **Fig. 3. Enabling technology: substrate/interface engineering.** (A) SEM images showing the

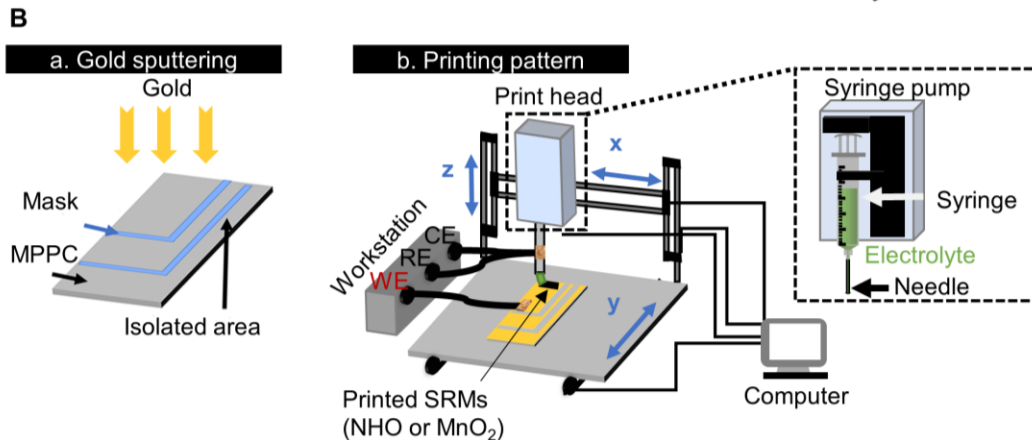
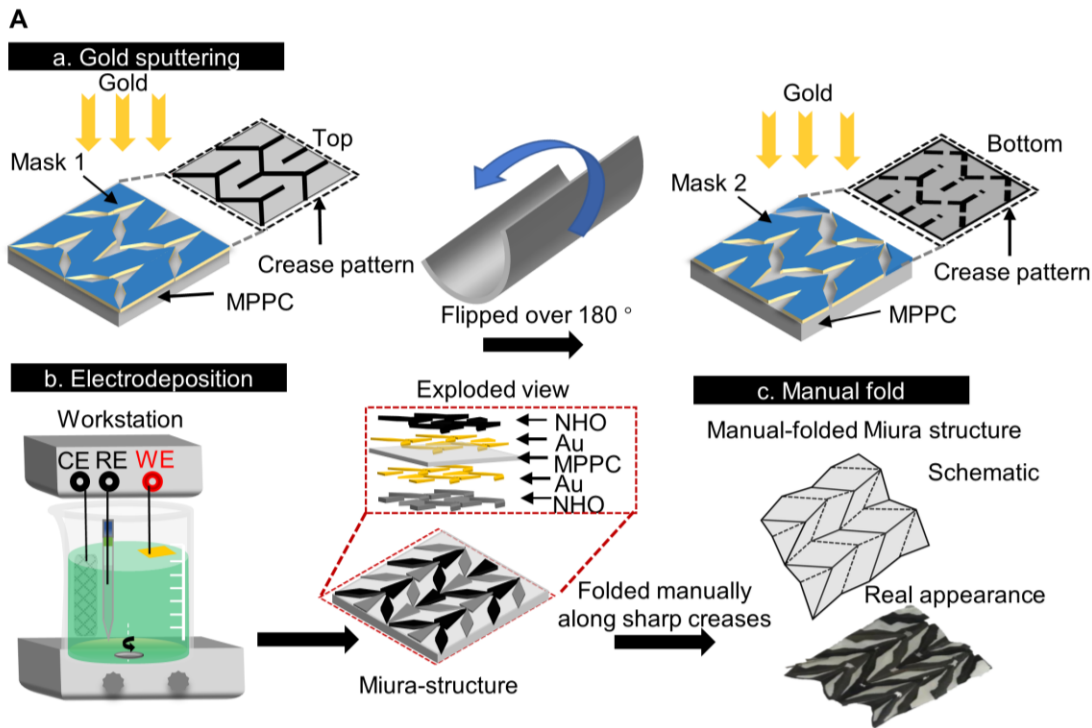
5 pores filling process at (i) 0.5 h and (ii) 2 h during electrodeposition of NHO. Scale bar: 2 μm . (B)

6 Effect of pore sizes of MPPC on the actuation performance and structural integrity; inset: an

7 actuator made by electrodepositing NHO on a non-porous PC membrane substrate for 0.5 h with

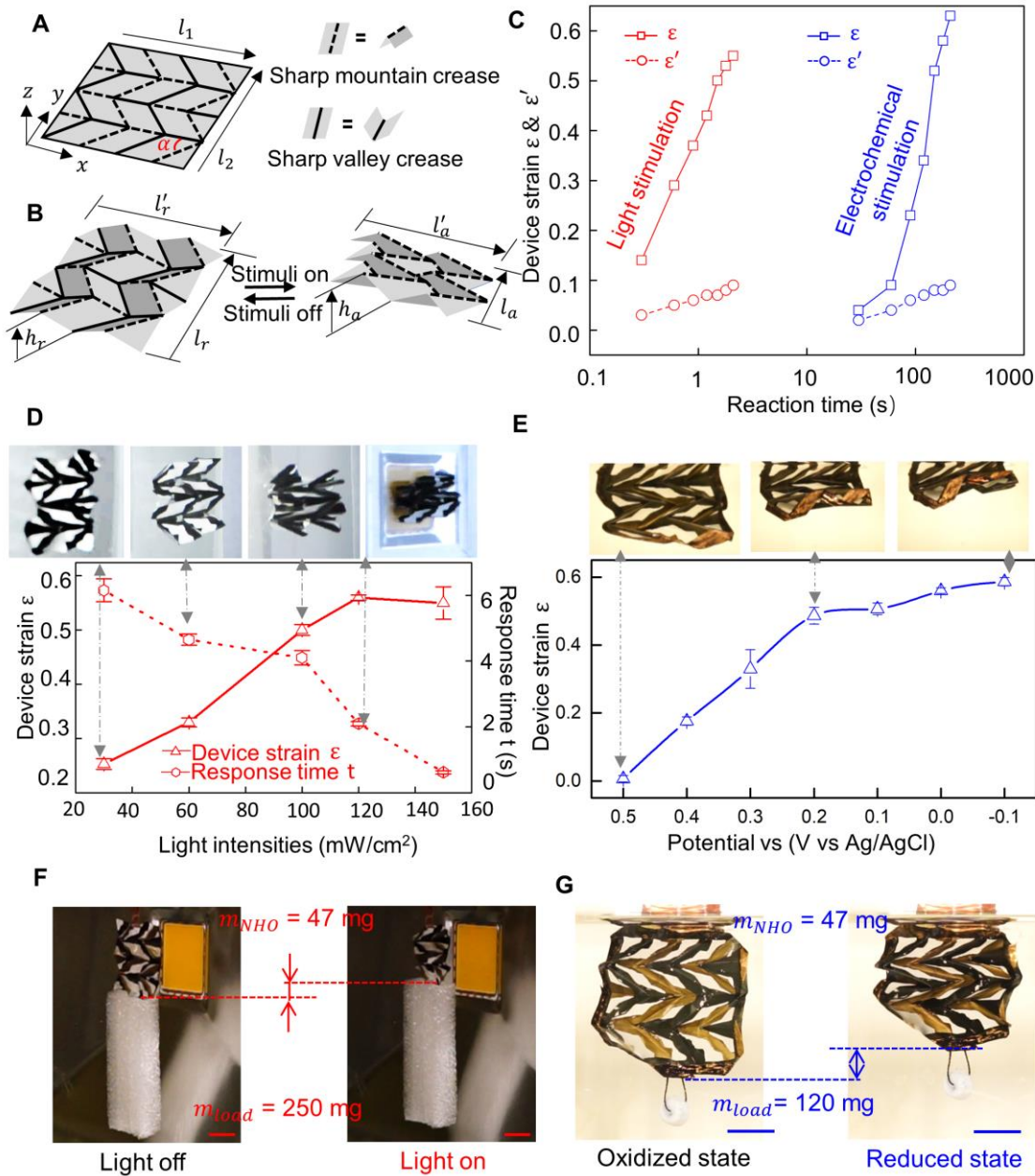
8 significant delamination just after 5 cycles, scale bar: 5 mm. (C) Device bending angle change

1 over 3000 cycles. The electrochemical actuation test was performed under step potential from 1 V
 2 for 1 s to -1 V for 1 s in 1 M NaOH; the light actuating was performed under the light intensity of
 3 $\sim 20 \text{ mW/cm}^2$. **(D)** Bending curvature change κ vs $\frac{6h_a(h_a + h_s)}{E_a h_a^3 + E_s h_s^3}$ for NHO electrodeposited on
 4 MPPC and on Ni substrates [21] under electrochemical actuation in 1 M NaOH electrolyte, and
 5 light actuation under visible light of around 20 mW/cm^2 . Inset: schematic diagram of an actuator
 6 at recovered and actuated state.



7

1 **Fig. 4. Enabling technology: Pattern fabrication of SRM.** (A) Two-sided, mask-based bath-
 2 electrodeposition. (B) Direct SRM pattern printing on Au-sputtered areas of MPPC membranes
 3 by a microfluidic electrochemical writing method.

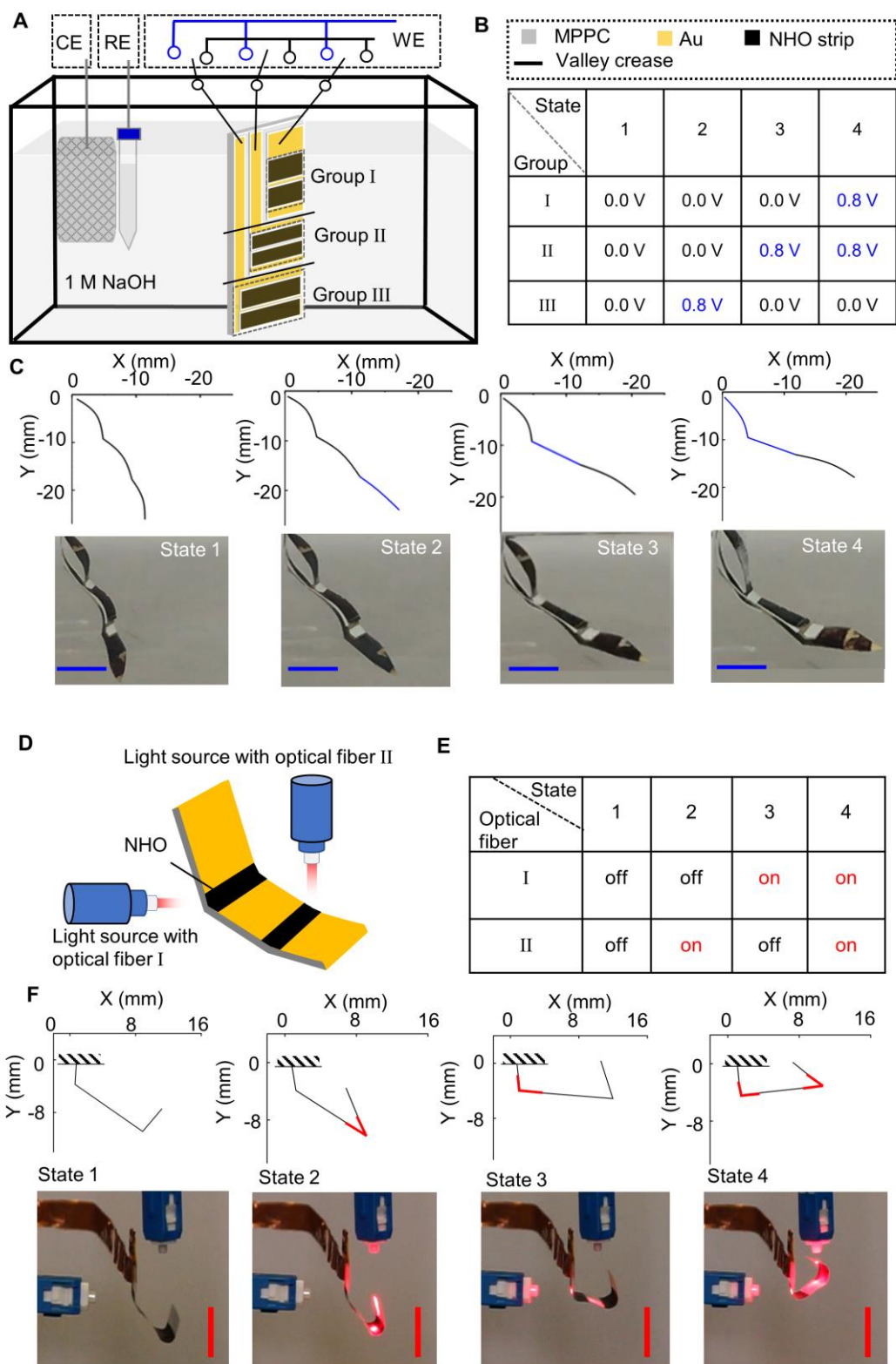


4
 5
 6 **Fig. 5. Light (red) and voltage (blue) triggered actuation of self-actuating Miura structure**
 7 **based on sharp NHO creases.** (A-B) Schematic of Miura fold. (A) Sharp-crease design for the
 8 Miura structure, with dashed line for sharp mountain creases and solid line for sharp valley
 9 creases. (B) Schematic Miura fold at recovered (stimuli off) and actuated (stimuli on) states.
 10 Widths l_r and l_a in the recovered and actuated states, respectively, define the device strain ϵ

1 along the l_2 direction according to $\varepsilon = (l_r - l_a)/l_r$. Device strain ε' perpendicular to the l_2
2 direction is defined as $\varepsilon' = (l'_r - l'_a)/l'_r$. **(C)** Experimental device strains ε and ε' along and
3 perpendicular to the l_2 direction, respectively, vs time, under light stimulation at ~ 120 mW/cm²
4 intensity (red), and electrochemical stimulation with potential -0.2 V applied relative to Ag/AgCl
5 electrode in 1M NaOH electrolyte (blue). Time zero refers to the moment the stimulation was
6 switched on. **(D)** Device strain ε along l_2 and response time of Miura micro-robot at different
7 light intensities from 30 mW/cm² to 150 mW/cm². **(E)** Device strain ε along l_2 direction in
8 response to varying potential from 0.5 V (oxidized state) to -0.1V (reduced state) with a slow scan
9 rate of -3mV/s to maintain quasi equilibrium at each potential value. **(F, G)** Miura lift: **(F)** under
10 light stimulation at 120 mW/cm² intensity (load: 250 mg), see Movie S7 for details; **(G)** under
11 electrochemical stimulation by potential -1 V relative to Ag/AgCl electrode in 1M NaOH
12 electrolyte (load: ~ 120 mg after accounting for buoyancy). See Movie S8 for details.

13

14



1

2 **Fig. 6. Electrochemically and light triggered micro-robotic fingers with independently**
 3 **controlled muscle groups.** (A~C) Electrochemically stimulated finger. (A) Schematic diagram
 4 and actuation set-up of the printed finger comprising three independently controlled muscles. (B)

1 Exemplary control states of voltage signals (values in volts). (C) Actual motion of the robotic
2 finger with NHO muscles under the four exemplary states illustrated in (B), scale bar: 10 mm, and
3 see Movie S9 for details. (D~F) Locally light stimulated finger. (D) Schematic diagram and
4 actuation set-up of finger comprising two independently controlled hinges stimulated locally by
5 two light sources with optical fibers at light intensity $\sim 30 \text{ mW/cm}^2$. (E) Exemplary control states
6 of light signals. (F) Actual motion of robotic finger with NHO hinges under the four exemplary
7 states illustrated in (E), scale bar: 10 mm, see Movie S10 for details.

8

9 **Additional information**

10 Section S1. Intrinsic actuation stress from bending curvature

11 Section S2. Electrochemical actuation

12 Section S3. Light actuation

13 Fig. S1. The schematic diagrams of a bi-layered actuator.

14 Fig. S2. Actuating performance of NHO under different fabrication conditions.

15 Fig. S3. The best performing electrochemical NHO actuator.

16 Fig. S4. Electrochemically triggered micro-robots made by printed MnO_x .

17 Fig. S5. Light actuation test setup.

18 Fig. S6. Cathodic current peak and curvature at different scan rate.

19 Fig. S7. Curvature at scan rate ranging from 25 mV/s to 250 mV/s.

20 Fig. S8. Bending angle of single origami crease hinge over 1000 cycles.

21 Table S1: A summary of origami actuators fabricated by stimuli-responsive materials.

22 Movie S1. A robotic hand with independently printed and controlled MnO_x finger hinges,
23 stimulated in 0.5 M Na_2SO_4 , with each finger under step potential 0 V to actuate and 1 V to
24 recover. (Play speed: $\times 2$)

1 Movie S2. Actuating performance of the NHO cantilever actuator in 1 M NaOH solution cyclic
2 with a scan rate of 25 mV/s with potential window of 0.8 V. (Play speed: $\times 5$)
3 Movie S3. Single smooth NHO fold in response to light (play speed: $\times 3$) and electrochemical
4 stimulations. (Play speed: $\times 8$)
5 Movie S4. Light stimulated Miura fold based on NHO creases. (Play speed: $\times 1$)
6 Movie S5. Fast response and light stimulated Miura fold based on NHO creases under light
7 intensity 150 mW/cm². (Play speed: $\times 1$)
8 Movie S6. Electrochemically stimulated Miura fold based on NHO creases with step potential (-
9 0.2 V) to actuate and (0.8 V) to recover. (Play speed: $\times 25$)
10 Movie S7. Light stimulated Miura structure based on NHO creases lifts a load (~ 250 mg) under
11 light intensity of 120 mW/cm². (Actuating process: play speed: $\times 1$; relaxing process: play speed
12 $\times 5$)
13 Movie S8. Electrochemically stimulated Miura structure based on NHO creases lifts a load (~ 120
14 mg after accounting for buoyancy) with step potential (-1 V). (Play speed: $\times 25$)
15 Movie S9. Printed actuator with three independently controlled NHO muscles groups, mimicking
16 the finger movements. (Play speed $\times 4$)
17 Movie S10. Finger geometry with two independently local controlled NHO hinges stimulated
18 locally by light. (Actuating process: play speed: $\times 1$; recovering process: play speed $\times 2$)
19 Movie S11. The curling actuating performance of printed MnO_x actuator in 0.5 M Na₂SO₄ under
20 different step-potential stimulations. (Play speed: $\times 2$)
21 Movie S12. Smooth NHO Yoshimura unit fold under various light intensities. (Play speed: $\times 5$)
22
23
24
25
26

1
2 **SUPPLEMENTARY MATERIALS**

3 Section S1. Intrinsic actuation stress from bending curvature

4 Section S2. Electrochemical actuation

5 Section S3. Light actuation

6 Fig. S1. The schematic diagrams of a bi-layered actuator.

7 Fig. S2. Actuating performance of NHO under different fabrication conditions.

8 Fig. S3. The best performing electrochemical NHO actuator.

9 Fig. S4. Electrochemically triggered micro-robots made by printed MnO_x .

10 Fig. S5. Light actuation test setup.

11 Fig. S6. Cathodic current peak and curvature at different scan rate.

12 Fig. S7. Curvature at scan rate ranging from 25 mV/s to 250 mV/s.

13 Fig. S8. Bending angle of single origami crease hinge over 1000 cycles.

14 Table S1: A summary of origami actuators fabricated by stimuli-responsive materials.

15 Movie S1. A robotic hand with independently printed and controlled MnO_x finger hinges,
16 stimulated in 0.5 M Na_2SO_4 , with each finger under step potential 0 V to actuate and 1 V to
17 recover. (Play speed: $\times 2$)

18 Movie S2. Actuating performance of the NHO cantilever actuator in 1 M NaOH solution cyclic
19 with a scan rate of 25 mV/s with potential window of 0.8 V. (Play speed: $\times 5$)

20 Movie S3. Single smooth NHO fold in response to light (play speed: $\times 3$) and electrochemical
21 stimulations. (Play speed: $\times 8$)

22 Movie S4. Light stimulated Miura fold based on NHO creases. (Play speed: $\times 1$)

23 Movie S5. Fast response and light stimulated Miura fold based on NHO creases under light
24 intensity 150 mW/cm^2 . (Play speed: $\times 1$)

25 Movie S6. Electrochemically stimulated Miura fold based on NHO creases with step potential (-
26 0.2 V) to actuate and (0.8 V) to recover. (Play speed: $\times 25$)

1 Movie S7. Light stimulated Miura structure based on NHO creases lifts a load (~250 mg) under
2 light intensity of 120 mW/cm^2 . (Actuating process: play speed: $\times 1$; relaxing process: play speed
3 $\times 5$)

4 Movie S8. Electrochemically stimulated Miura structure based on NHO creases lifts a load (~120
5 mg after accounting for buoyancy) with step potential (-1 V). (Play speed: $\times 25$)

6 Movie S9. Printed actuator with three independently controlled NHO muscles groups, mimicking
7 the finger movements. (Play speed $\times 4$)

8 Movie S10. Finger geometry with two independently local controlled NHO hinges stimulated
9 locally by light. (Actuating process: play speed: $\times 1$; recovering process: play speed $\times 2$)

10 Movie S11. The curling actuating performance of printed MnO_x actuator 0.5 M Na_2SO_4 under
11 different step-potential stimulations. (Play speed: $\times 2$)

12 Movie S12. Smooth NHO Yoshimura unit fold under various light intensities. (Play speed: $\times 5$)

13

1 Supplementary Materials

2 Section S1. Intrinsic actuation stress from bending curvature

3 Here, the intrinsic actuating stress characteristics of the active NHO material are analyzed by
4 Timoshenko's theory [31]. The configuration analyzed is shown in fig. S1, where an active
5 actuating layer expands, causing the underneath passive layer to bend. The thin Au pre-sputtered
6 layer is ignored since its nanometric thickness is negligible compared with the micron-scale h_a
7 and h_s in the present experiments. As indicated in fig. S1B as the active layer attempts to expand
8 with an actuation force $P = P_a$ per unit width, the resultant effect on the underlying passive layer
9 is a tensile force of the same magnitude $P = P_s$. Therefore, the force couple P produces bending
10 moments $M_a = E_a I_a \kappa$ and $M_s = E_s I_s \kappa$ in each of the two layers, so that $P(h_a + h_s)/2 = (E_a I_a + E_s$
11 $I_s)\kappa$, where $I_a = h_a^3/12$ and $I_s = h_s^3/12$, E_a and E_s are Young's moduli of the active and substrate
12 layers respectively, and κ is the bending curvature. The average actuation stress $\sigma_a = P/h_a$ exerted
13 by the active layer is therefore

$$14 \quad \kappa = \frac{6h_a(h_a + h_s)}{E_a h_a^3 + E_s h_s^3} \sigma_a \quad (S1)$$

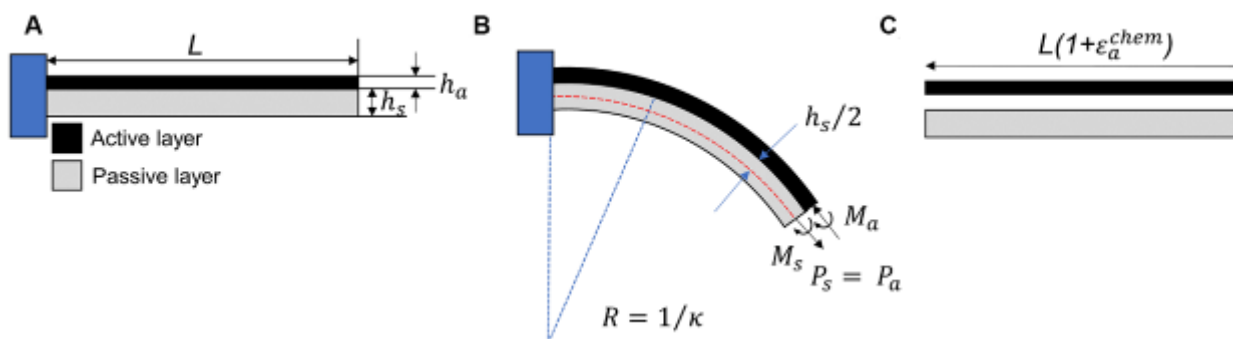
15 In the active layer, a chemical, plastic strain ε_a^{chem} acts to cause the actuation, and this plays
16 the role of the mismatch strain in Timoshenko's theory, i.e. when the actuating layer is freed out
17 from the substrate, it will be longer than the substrate by strain ε_a^{chem} as shown in fig. S1C.
18 Timoshenko gave this strain as:

$$19 \quad \varepsilon_a^{chem} = \left[\frac{h_a + h_s}{2} + \frac{E_a h_a^3 + E_s h_s^3}{6(h_a + h_s)} \left(\frac{1}{E_a h_a} + \frac{1}{E_s h_s} \right) \right] \kappa = \left[\frac{1}{E_a} + \frac{h_a}{E_s h_s} + \frac{3h_a(h_a + h_s)^2}{E_a h_a^3 + E_s h_s^3} \right] \sigma_a \quad (S2)$$

20 The work density U of the actuating mechanism is $U = \int \sigma_a d\varepsilon_a^{chem}$, or, from Eq. (S2),

$$21 \quad U = \frac{\sigma_a^2}{2} \left[\frac{1}{E_a} + \frac{h_a}{E_s h_s} + \frac{3h_a(h_a + h_s)^2}{E_a h_a^3 + E_s h_s^3} \right] \quad (S3)$$

22

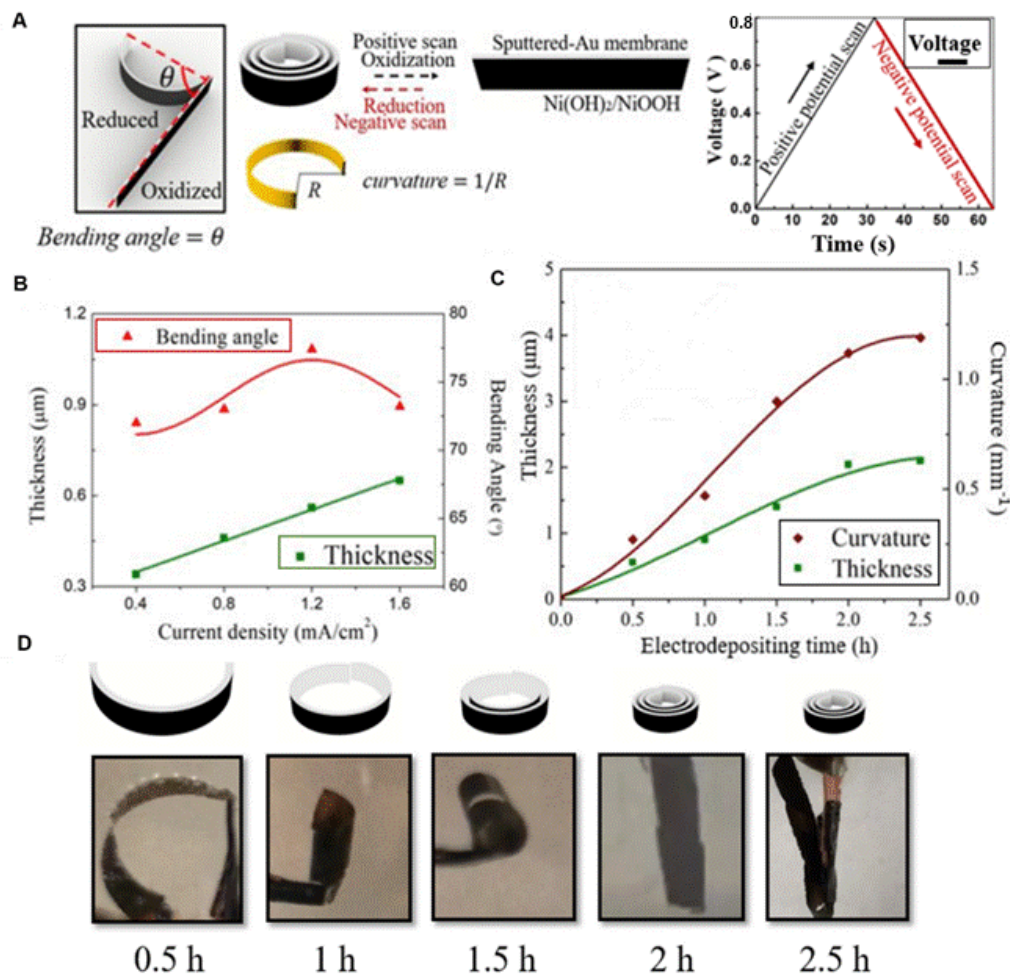


1
2 **Fig. S1. The schematic diagrams of a bi-layered actuator (A)** when the actuating layer is in the
3 oxidized state; **(B)** when the actuating layer is in the reduced state; **(C)** if the actuating layer was
4 freed from the substrate.

6 Section S2. Electrochemical actuation

7 To measure the intrinsic actuation stress of the NHO material under electrochemical
8 stimulation, NHO films of different thicknesses h_a were fabricated on 10 μm thick (h_s) MPPC
9 membranes by bath electrodeposition (see Materials and Methods). Electrochemical actuation
10 tests were then carried out in 1 M NaOH electrolyte (see Materials and Methods). As shown in
11 fig. S2A, the actuator exhibited large curling motion towards the membrane side when reduced
12 (during negative potential scan) and straightened or even curled backward to the side of the active
13 material when oxidized (during positive potential scan). This corresponds to the actuating layer
14 expanding during reduction and contracting during oxidation. To optimize the electrodeposition
15 conditions for NHO, the effects of the electrodeposition current density were first investigated. At
16 an electrodepositing time of 0.5 h, fig. S2B shows direct linearity between the thickness of the
17 electrodeposited NHO layer and the current density. The average bending angle of the first five
18 actuation cycles first increases with the current density and then drops beyond 1.2 mA/cm^2 , due
19 likely to the poor adhesion of the NHO layer on the Au-sputtered MPPC membrane at the highest
20 electrodepositing current density of 1.6 mA/cm^2 , as evidenced by the occasional observation of
21 the layer peeling off from the membrane. Therefore, the optimized current density is selected to

1 be 1.2 mA/cm^2 . Figure S2C shows the effect of the electrodepositing time at current density of 1.2
 2 mA/cm^2 , on the thickness of the NHO layer and also the subsequent actuation maximum
 3 curvature. The results show that both the thickness of the actuating layer and the actuating
 4 curvature first increase approximately proportionally with the electrodepositing time but then
 5 saturate to steady values for the times larger than 2 h. The typical largest curvatures achieved over
 6 the potential scan covering the redox regime at different electrodepositing times are shown in fig.
 7 S2D.



8
 9 **Fig. S2 Actuating performance of NHO under different fabrication conditions.** (A)
 10 Schematic showing bending angle and curvature during negative and positive potential scan (the
 11 active material layer is drawn as black, while the substrate is white). (B) Effects of current density
 12 for 0.5 h on thickness of electrodeposited $\text{Ni(OH)}_2/\text{NiOOH}$ layer and subsequent actuation

1 bending. (C) Effects of electrodepositing time on the typical largest curvature. (D) Typical largest
2 curvature during electrodeposition time ranging from 0.5 h to 2.5 h.

3 The data in fig. S2C are replotted in Fig. 3D of the main text as curvature κ vs

4 $\left[\frac{6h_a(h_a + h_s)}{E_a h_a^3 + E_s h_s^3} \right]$, according to the format suggested by Eq. (S1). Here, the h_s for the MPPC

5 substrates is fixed at 10 μm , $E_s = 2.3$ GPa, $E_a = 24 \pm 5.6$ GPa by nanoindentation tests (see

6 Materials and Methods), and h_a varies between 0.6 to 2.2 μm . As mentioned above, the Au layer

7 deposited on top of the MPPC membrane is ignored since it is very thin at just 14 nm (see

8 Materials and Methods). In addition, data from an earlier report [21] for NHO on Ni substrates are

9 also plotted, where the NHO thickness was constant at 0.44 μm , the Ni substrate thickness h_s

10 varied from 1.2 to 5.5 μm , and $E_s = 220$ GPa for Ni. The original device strains (D/L) reported in

11 [21], where D is end-deflection of the cantilever actuators of length L , are converted into bending

12 curvature κ by using the geometrical relation $\kappa = 2(D/L) / \left\{ L \left[1 + (D/L)^2 \right] \right\}$ which gives

13 sufficient accuracy for the range studied. The plot indicates that Eq. (S1) is obeyed for both the

14 current NHO-on-MPPC actuators as well as the previous NHO-on-Ni ones, with a fairly constant

15 σ_a of 20 MPa. It is also intriguing to see that the NHO material is delivering such a constant

16 intrinsic actuating stress over a large curvature range, from nearly zero to about 1.2 mm^{-1} . The

17 actuating stress of ~ 20 MPa here is large among electrochemical actuators [40].

18 *Best electrochemical actuation performance* – In Fig. 3D of the main text, the largest

19 actuation curvature achieved in the present work is 1.2 mm^{-1} , with the NHO layer

20 electrodeposited for 2 h (fig. S2C). Figure S3 and Movie S2 show the typical actuation of this

21 actuator, of size measuring 15 mm \times 3 mm. During the negative potential scan in the latter half of

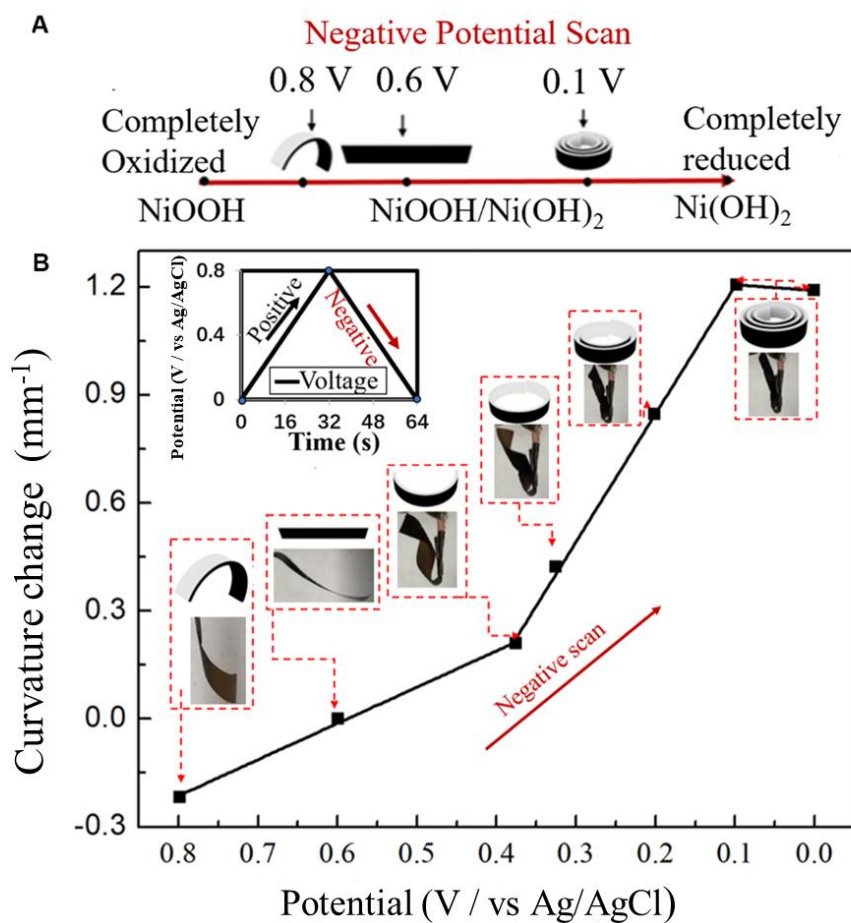
22 the potential cycle, the curvature increased rapidly after ~ 0.4 V, due to the reduction reaction of

23 NiOOH into Ni(OH)₂, leading to large expansion of the active layer. The actuator also exhibited a

24 slight twisting motion, possibly due to the slightly uneven deposition of the actuating material. At

1 the end of the negative scan, the actuator underwent a cumulative angular deflection of $>1000^\circ$
2 (i.e. 2.8 revolutions) at the free-end, and from this, the curvature is estimated at 1.2 mm^{-1} . The
3 actuation strain ε_a^{chem} calculated from Eq. (S2) is 1%, and the work density calculated from Eq.
4 (S3) is $U = 97 \text{ kJ/m}^3$.

5 Therefore, in summary, the present NHO material can deliver a constant actuating stress of
6 $19.5 \pm 0.5 \text{ MPa}$ over strains up to 1%, and work density up to $\sim 100 \text{ kJ/m}^3$. The maximum work
7 density here already outperforms human skeletal muscles ($\sim 40 \text{ kJ/m}^3$) [32] and is comparable to
8 that of typical metallic muscles [53]. Although it is smaller than ferroelectric polymers actuators
9 ($\sim 1 \text{ MJ/m}^3$) [32] and the best nanoporous noble alloys ($\sim 6 \text{ MJ/m}^3$) [54], the NHO material is a lot
10 cheaper than nanoporous noble metals, and the triggering voltage needed is under 1 volt, which is
11 much lower than that of ferroelectric polymers (typically $>1 \text{ kV}$). The actuating stress of $\sim 20 \text{ MPa}$
12 here should be an intrinsic property of the NHO material at room temperature, but the maximum
13 strain and work density are only for the present actuator configurations. From Eq. (S1), the
14 curvature should further increase by increasing the thickness of the active layer, or decreasing the
15 stiffness of the substrate. However, the maximum thickness of the NHO layer that can be
16 achieved by the present fabrication method is about $2 \mu\text{m}$ even after prolonged electrodeposition
17 (fig. S2C), and this is already the case for the best performing actuator shown in fig. S3.
18 Therefore, further increase in actuation can only be achieved by using even softer or thinner
19 substrates. As the unit cell volume of Ni(OH)_2 is known to contract by approximately 10% when
20 it is oxidized into NiOOH [29, 55] further improvements of the actuating strain are highly
21 possible by using more compliant substrates.

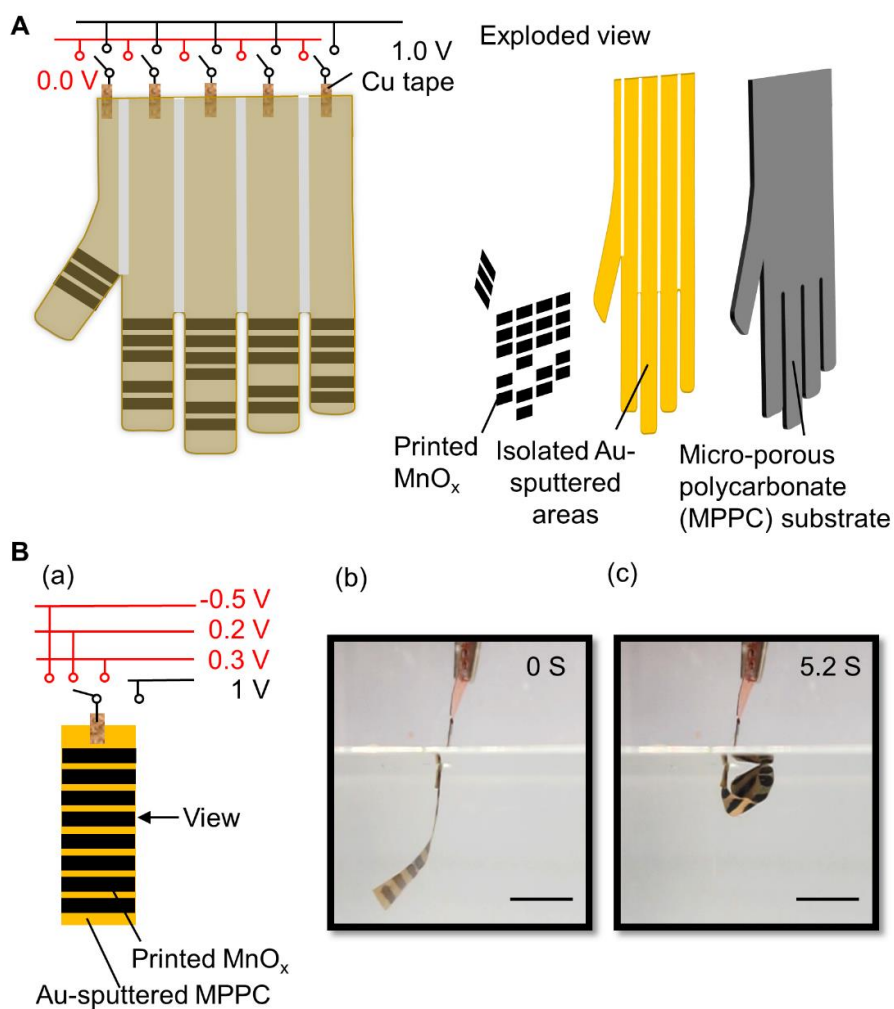


1

2 **Fig. S3. The best performing electrochemical NHO actuator.** (A) Curvature change trend from
 3 oxidized state to reduced state (half reduced cycle). (B) Curvature change during negative scan
 4 (half reduced cycle) from 0.8 V to 0 V at 25 mV/s. See Movie S2 for details.

5 To demonstrate the wide applicability of the two technical advancements discussed in the
 6 Section 2, another proven electrochemically stimulated material MnO_x [23] was also used to
 7 make actuating creases with the same micro-fluidic electrochemical printing and micro-riveting
 8 strategies (see Fig. 4B, and Materials and Methods). The printed actuating patterns of MnO_x
 9 demonstrate good adhesion with the porous polymeric substrate, thus proving the versatility of the
 10 micro-riveting and the microfluidic printing strategies. Results show that, by printing several
 11 parallel MnO_x actuating strips on the polymeric substrate, the printed actuator was able to
 12 demonstrate large curling motion during the redox reaction, as shown in fig. S4. For the same
 13 curling actuator, by applying different step potentials, the curling speed can be modified. By

1 comparing the same curling range, the curling speeds for different step-potential changes are:
 2 ~12 deg/s from 1V to 0.3 V, 19 deg/s from 1 V to 0.2 V, and 30 deg/s from 1 V to -0.5 V. Fig.
 3 S4B and Movie S11 show the fast response achieved by step potentials of 1 V to recover and -0.5
 4 V to actuate.

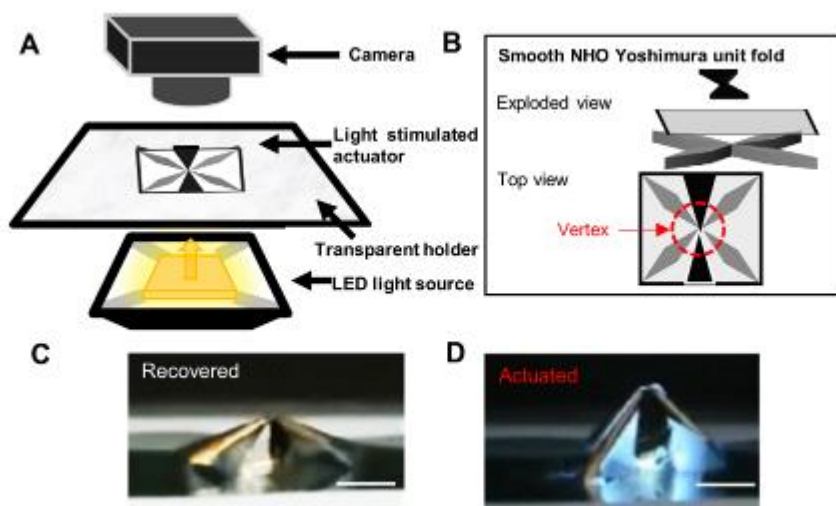


6
 7 **Fig. S4. Electrochemically triggered micro-robots made by printed MnO_x.** (A) Schematic
 8 diagram of the printed MnO_x full hand comprising five independently controlled fingers. (B)
 9 Curling actuator. (a) Schematic diagram of the printed MnO_x curling actuator. (b) Recovered state
 10 under step potential of 1 V relative to Ag/AgCl electrode in 0.5 M Na₂SO₄. (c) Actuated state
 11 under step potential of -0.5 V relative to the same electrode and in the same electrolyte. Scale bar:
 12 5 mm.

Section S3. Light actuation

To determine the typical σ_a of the NHO material on light stimulation, NHO films of various thicknesses h_a from 0.6 to 2.1 μm were bath-electrodeposited on MPPC membranes with $h_s = 10$ μm at an optimized current density of ~ 1.2 mA/cm^2 (see Materials and Methods). Light stimulation tests were carried out on the actuators (15 mm \times 3 mm) under a visible light intensity of ~ 20 mW/cm^2 . The actuators exhibited curling motion towards the NHO side in response to the light illumination, and started to straighten back to the side of the membrane when the light source was removed. This corresponds to the actuating layer contracting due to water desorption [22] under light illumination, and recovery due to water absorption [22] when the light is turned off. The curvature κ data are also plotted in Fig. 3D (in red) of the main text vs the factor $\left[\frac{6h_a(h_a + h_s)}{E_a h_a^3 + E_s h_s^3} \right]$. Linearity is observed as in agreement with Eq. (S1), and the slope indicates a value of 10.8 MPa for σ_a under ~ 20 mW/cm^2 visible light illumination. The largest actuation curvature change is 0.6 mm^{-1} for the thickest NHO layer of 2.1 μm tested. The corresponding light stimulated actuation strain is 0.5% as calculated by Eq. (S2), with the work density being 28 kJ/m^3 from Eq. (S3). Therefore, under visible light illumination at ~ 20 mW/cm^2 , the present NHO material can deliver a constant actuating stress of ~ 11 MPa, with strains up to $\sim 0.5\%$ and work density up to 28 kJ/m^3 .

Light actuation test setup – Light stimulation experiments in Figs. 1B, 3 and 5 of main text were carried out using a setup illustrated in fig. S5A (see Methods for details). Figures S5C and D show the application to the example of a Yoshimura origami unit [51] involving two smooth NHO valley creases (black) and four mountain creases (gray) (fig. S5B). Under light illumination at 40 mW/cm^2 , the actuator underwent self-folding in around 10 seconds as shown in fig. S5C and D, and at a higher light intensity of 100 mW/cm^2 , the self-folding process could be completed much quicker in around 4 seconds (see Movie S12).



1

2 **Fig. S5. Light actuation test setup.** (A) Schematic of light stimulation of origami actuators. (B)

3 Schematic of Yoshimura unit comprising smooth NHO valley and mountain creases. (C and D)

4 Light stimulated response of an actual self-actuating Yoshimura unit at recovered (C) and

5 actuated (D) states at light intensity of 40 mW/cm^2 (scale bar: 5 mm).

6

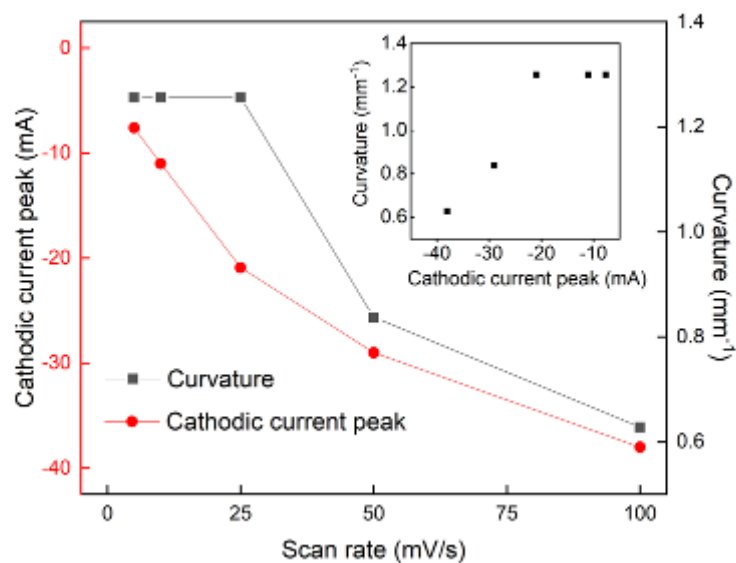
7

8

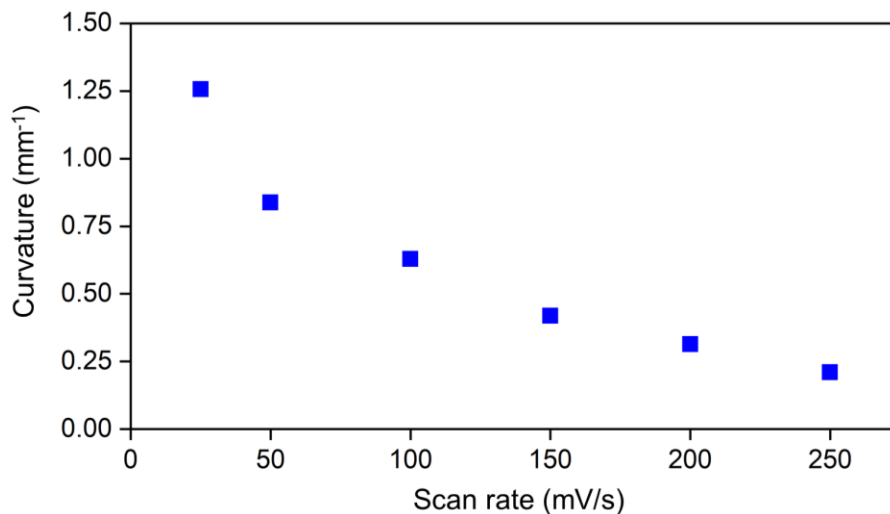
9

10

11

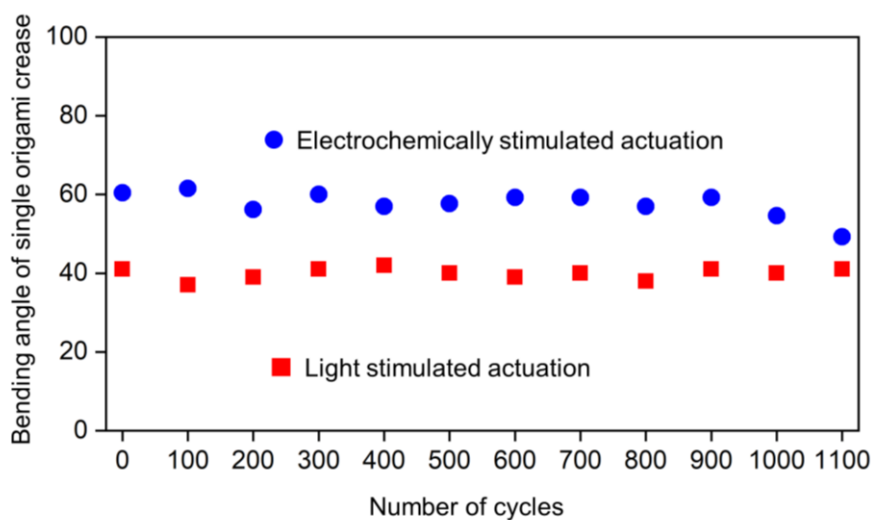


1
 2 **Fig. S6. Cathodic current peak and curvature at different scan rate**, with the inset showing
 3 the curvature vs the cathodic current peak.



5
 6 **Fig. S7. Curvature at scan rate ranging from 25 mV/s to 250 mV/s.** A fixed potential range of
 7 -0.2 V to 0.6 V was applied in 1 M NaOH electrolyte. The sample used here was the actuator that
 8 was electrodeposited for two hours on the substrate with pore size of 0.2 μm .

9



1

2 **Fig. S8. Bending angle of single origami crease hinge over 1000 cycles**, with a single crease
 3 triggered by step potential under -1 V for 0.5 s to actuate and 1 V for 1 s to recover in 1 M NaOH
 4 electrolyte and under illumination of vis light intensity at $\sim 25 \text{ mW/cm}^2$ on for 0.5 s to actuate and
 5 1 s off to recover for both 1000 times.

6

7

8

9

10

11

12

13

14

15

16

17

18

1 Table S1: A summary of origami actuators fabricated by stimuli-responsive materials.

Materials	Response time	Fabrication complexity and costs	Stimuli	Reference
Shape memory polymers	Slow in terms of hours	Easy and cheap	Water (recovered by acetone)	[13]
Shape memory polymers and hydrogels	Slow in terms of hours	Relatively complex but cheap	Water combined with temperature	[14]
Shape memory polymers	Slow in tens of minutes	Easy and cheap	Temperature	[15]
Temperature-sensitive hydrogels	Slow in terms of minutes	Relatively complex but cheap	Temperature	[16]
Liquid-crystal elastomers	Fast in terms of several seconds	Relatively complex requiring programming process but cheap	Temperature	[17]
shape memory polymer fibers	Slow in terms of minutes	Easy and cheap	Temperature	[18]
Graphene oxide and reduced graphene oxide	Fast in terms of seconds	Complex and expensive	NIR light	[20]
Transition metal hydroxides/oxides	Fast in terms of ~2 seconds for light stimulation; Slow in terms of a few to tens of minutes for electrochemical stimulation.	Easy and cheap	Low-intensity vis light (~1 sun) or mild electrochemical potential (< 1 V)	Present work

2
3
4
5
6
7
8

1 **Movies S1 to S12**

2 Movie S1. A robotic hand with independently printed and controlled MnO_x finger hinges,
3 stimulated in 0.5 M Na_2SO_4 , with each finger under step potential 0 V to actuate and 1 V to
4 recover. (Play speed: $\times 2$)

5 Movie S2. Actuating performance of the NHO cantilever actuator in 1 M NaOH solution cyclic
6 with a scan rate of 25 mV/s with potential window of 0.8 V. (Play speed: $\times 5$)

7 Movie S3. Single smooth NHO fold in response to light (play speed: $\times 3$) and electrochemical
8 stimulations. (Play speed: $\times 8$)

9 Movie S4. Light stimulated Miura fold based on NHO creases. (Play speed: $\times 1$)

10 Movie S5. Fast response and light stimulated Miura fold based on NHO creases under light
11 intensity 150 mW/cm^2 . (Play speed: $\times 1$)

12 Movie S6. Electrochemically stimulated Miura fold based on NHO creases with step potential (-
13 0.2 V) to actuate and (0.8 V) to recover. (Play speed: $\times 25$)

14 Movie S7. Light stimulated Miura structure based on NHO creases lifts a load (~ 250 mg) under
15 light intensity of 120 mW/cm^2 . (Actuating process: play speed: $\times 1$; relaxing process: play speed
16 $\times 5$)

17 Movie S8. Electrochemically stimulated Miura structure based on NHO creases lifts a load (~ 120
18 mg after accounting for buoyancy) with step potential (-1 V). (Play speed: $\times 25$)

19 Movie S9. Printed actuator with three independently controlled NHO muscles groups, mimicking
20 the finger movements. (Play speed $\times 4$)

21 Movie S10. Finger geometry with two independently local controlled NHO hinges stimulated
22 locally by light. (Actuating process: play speed: $\times 1$; recovering process: play speed $\times 2$)

23 Movie S11. The curling actuating performance of printed MnO_x actuator in 0.5 M Na_2SO_4 under
24 different step-potential stimulations. (Play speed: $\times 2$)

1 Movie S12. Smooth NHO Yoshimura unit fold under various light intensities. (Play speed: ×5)